Journal of Energy Storage 153 (2026) 120819

Contents lists available at ScienceDirect

Journal of Energy Storage

journal homepage: www.elsevier.com/locate/est

Research papers

Optimal operation of off-grid integrated hydrogen energy utilization systems: Life-cycle cost reduction considering waste heat recovery☆

Shihao Zhu [a], Banghua Du [b], Peipei Meng [a], Xinyu Lu [c], Yang Li [d], Changjun Xie [a,b,*], Leiqi Zhang [e], Bo Zhao [e]

[a] School of Automation, Wuhan University of Technology, Wuhan, 430070, China
[b] Hubei Key Laboratory of Advanced Technology for Automotive Components, Wuhan University of Technology, Wuhan, 430070, China
[c] School of Energy and Power Engineering, Huazhong University of Science and Technology, Wuhan, 430074, China
[d] Department of Electrical Engineering, Chalmers University of Technology, Gothenburg, 41258, Sweden
[e] State Grid Zhejiang Electric Power Research Institute, Hangzhou, 310014, China

ARTICLE INFO

Keywords:
Integrated hydrogen energy utilization system
Operation optimization
Hydrogen energy storage
Life cycle cost

ABSTRACT

The integrated hydrogen energy utilization system (IHEUS) exhibits great potential for microgrid applications. However, its practical deployment faces significant challenges, primarily due to the low energy conversion efficiency and rapid aging of electrolyzers and fuel cells, especially when handling highly fluctuating power flows. To address these issues, this study proposes a multi-objective optimal dispatch scheme for off-grid IHEUS operations, incorporating waste heat recovery and life cycle cost considerations. First, a mechanistic model is established to characterize the electric-hydrogen-heat output characteristics of the system, with a specific focus on waste heat recovery and utilization subsystems. By correlating the aging behavior and lifetime degradation to voltage decay, a life-cycle operational cost function is formulated for the multi-objective optimization (MOO) model. Within this framework, comprehensive energy efficiency and energy supply loss probability are adopted as performance metrics to enhance energy utilization and stability. The resulting MOO problem is solved and prioritized using a proposed NSGA-III combined entropy-weighted TOPSIS strategy. Comparative studies demonstrate that this strategy effectively identifies the optimal dispatch scheme, achieving operational cost reductions of at least 17.53%, comprehensive energy efficiency improvements ranging from a 0.13% decrease to a 0.61% increase, and a limited increase in energy supply loss probability (4.14%).

1. Introduction

Microgrids in coastal and remote mountainous regions face limited connectivity to the main power grid owing to their adverse geographic and climatic conditions [1]. Due to insufficient support from the main grid, achieving a stable energy supply solely through renewable energy sources is unfeasible [2]. Given hydrogen's high energy density, long-duration storage capacity, and environmental friendliness, it emerges as a promising solution to address this challenge effectively [3–5].

1.1. Background and motivation

The integration of hydrogen energy into renewable energy microgrids forms traditional hydrogen-electric coupling systems, with hydrogen-electric coupling technology as the foundation for efficient application. In an environment with unstable renewable energy supply, the primary challenge for hydrogen-electric coupling technology is achieving stable and efficient operation of the hydrogen energy system [6]. Secondly, the comprehensive utilization of hydrogen energy is crucial for enhancing overall system efficiency. Hydrogen energy can be used not only for power generation but also through combined heat and power systems to provide thermal energy or as an industrial raw material, achieving multiple uses [7]. Therefore, effectively recovering and utilizing the waste heat generated by hydrogen energy equipment during operation within the microgrid system is an important research direction for improving energy utilization efficiency.

The aging of hydrogen energy equipment significantly affects system reliability and economic performance. Current research reveals that frequent start-stop cycles and high-frequency power fluctuations

☆ This article is part of a Special issue entitled: 'Hybrid Energy Storage' published in Journal of Energy Storage.

* Corresponding author at: School of Automation, Wuhan University of Technology, Wuhan, 430070, China.
E-mail address: jackxie@whut.edu.cn (C. Xie).

https://doi.org/10.1016/j.est.2026.120819
Received 27 July 2024; Received in revised form 18 November 2025; Accepted 27 January 2026
Available online 4 February 2026

Nomenclature

Subscripts and superscripts

WT	Wind turbine
in	Cut-in
out	Cut-off
r	Rate
PV	Photovoltaic
el	PEMEL
oc	Open-circuit
act	Activation polarization
con	Concentration difference
ohm	Ohmic resistance
0	Reference/Initial
an	Anode
ca	Cathode
max	Maximum
s	Stack
fc	PEMFC
tot	Total
HST	Hydrogen storage tank
HRS	Hydrogen refueling station
HT	Heat storage tank
TL	Thermal load
m	Maintaining
l	Low power fluctuation
h	High power fluctuation
sys	System
o&m	Operation and maintenance
deg	Degradation
rep	Replace
inv	Invest
eol	End of life
ini	Initial
fin	Final
re	Recycle
min	Minimum

Symbols

W	Solar radiation intensity, kW/cm^2
A	Area, cm^2
n	Amount of substance, mol
F	Faraday's constant, 96,485C/mol
R	Gas constant, 8.314 J/(mol·K)
p	Pressure, Pa
i	Current density, A/cm^2
T	Temperature, K
F	Molar flow rate, mol/s
H	Molar enthalpy, J/mol
Q	Heat, kJ
G	Gibbs free energy, 236.483 kJ/mol
S	Entropy, −164.025 J/(mol·K)
M	Molar mass, g/mol
C	Cost, ¥
LHV	Low heating value, 242 kJ/mol

Greek symbols

η	Efficiency
Δ	Variation
ξ	Empirical coefficient
α, β, and γ	O&M cost coefficient
ψ	Trade cost coefficient, ¥/Nm^3

accelerate the degradation of electrolyzers and fuel cells. Furthermore, optimization-based control strategies are crucial to achieving efficient and reliable operation of microgrid systems. Hydrogen-integrated microgrids encompass diverse energy forms and conversion processes, necessitating control frameworks that address multi-objective and multi-constraint complexities.

1.2. Literature review

Plenty of recent works have been focused on the research of hydrogen-supported microgrid systems in the form of hydrogen-electric or hydrogen-heat coupled systems. For example, Tahir et al. [8] proposed a globally applicable framework for hydrogen-based renewable energy systems involving 14 performance criteria, microgrid optimization tools, and a hybrid multi-criteria decision-making methodology. They demonstrated the effectiveness of the framework in an application in Pakistan, and the results showed that the levelized costs of electricity/hydrogen and carbon emissions were reduced. Sun et al. [9] proposed a networked hydrogen multi-energy microgrid operation plan and designed a nested decomposition algorithm based on stochastic dyadic dynamic integer programming. This approach transforms networked hydrogen multi-energy microgrid operation plan into a multi-stage stochastic mixed-integer program, facilitating to capture of the seasonal and intra-day dynamics of the system. The proposed stochastic dyadic dynamic integer programming demonstrated efficiency in solving the large-scale multi-stage stochastic mixed-integer program. Endo et al. [10] proposed a small-scale stationary hydrogen energy utilization system for renewable energy generation with compactness, safety, and mild operating conditions. After a 24-h controlled operation in a building energy management system, it was demonstrated that the proposed system could achieve near-zero power consumption and zero emissions. Integrating electric storage and heat-producing devices enhances system performance but increases complexity and capital investment, whereas relying solely on hydrogen energy can mitigate these issues.

On the contrary, integrated hydrogen energy utilization system (IHEUS) solely utilizes hydrogen energy converted from renewable sources, aiming to reduce the usage of electrochemical energy storage or extra heat generation. IHEUS is considered to be superior in terms of energy storage density, storage duration, and cleanliness [11,12], and many investigations have also been conducted. For example, Zhang et al. [13] introduced an electric hydrogen production scheme with the characteristics of fast response and long-duration energy storage, and numerical studies showed that this scheme can improve energy efficiency and alleviate the pressure on its natural gas pipeline network. Pan et al. [14] proposed an IHEUS planning model incorporating hydrogen production and storage technologies and used stochastic and robust optimization to address generation-load uncertainty. They found that IHEUS offers significant economic benefits at high levels of renewable energy penetration. Rabiee et al. [15] proposed a nonlinear programming model to assess how voltage safety, hydrogen facility location, and wind penetration affect green hydrogen production. They tested the model on the IEEE 39-bus system and found that IHEUS can stabilize microgrids and meet diverse energy demands through renewable energy and hydrogen equipment. In general, IHEUS can stabilize microgrids and meet diverse energy demands with its renewable energy and hydrogen systems, making it well-suited for off-grid operation. However, research on the coordinated operation of its various devices remains limited.

In IHEUS, rapid power fluctuations from renewable energy accelerate the degradation of electrolyzers and fuel cells. Studies show that frequent start-stop cycles, power fluctuations, and high-frequency current ripple increase the wear on PEMEL electrocatalysts, membranes, and cause metal ion poisoning [16,17]. In this respect, Frensch et al. [18] compared the performance change and aging trend of PEMEL over time under seven different operating conditions. They concluded that dynamic operation would lead to increased passivation of the catalyst carrier. Weiß et al. [19] proposed an accelerated stress test (AST) method for PEMELs that imitates fluctuating power sources and verified the negative impacts of frequent start-stop, power fluctuations, and prolonged PEMEL life for high-power operation. Similarly, proton-exchange-membrane fuel cells (PEMFC) will experience accelerated precipitation and corrosion of platinum on the electrodes under dynamic conditions, thus exacerbating membrane degradation [20,21]. In this respect, Dhimish et al. [22] found that after 180 days of continuous operation, PEMFC efficiency dropped by 7.2% due to voltage fluctuations and by 14.7% at higher temperatures. Ren et al. [23] examined the PEMFC's aging by the AST and specifically analyzed the mechanistic causes under various severe operating conditions. Therefore, to reduce IHEUS costs, it is crucial to design operation strategies that slow the aging of PEMEL and PEMFC by quantifying their aging processes. Currently, there is limited research on optimizing strategies to mitigate the impact of power fluctuations on device aging, which hinders overall IHEUS performance.

Beyond economic indicators, system energy efficiency and stability are crucial for IHEUS performance. Optimizing these metrics can significantly enhance overall system performance. For example, Li et al. [24] proposed a two-stage approach to validate IHEUS storage constraints and improve planning accuracy. Case studies showed it effectively reduced annual costs and battery capacity requirements, and significantly decreased average errors in data selection compared to traditional methods. Wang et al. [25] reported a collaborative planning method for siting and determining energy station (ES) and pipeline networks (PNs), solved using heuristic algorithms and PNs planning algorithms. It was empirically demonstrated to be effective in reducing the cost and load peak-to-valley differential rates. Ma et al. [26] proposed an optimal dispatch model of cogeneration based on electricity-to-gas conversion and carbon capture. By using YALMIP and GUROBI to solve the model, it was verified that the proposed method enhances the utilization of renewable energy and reduces carbon emissions and operating costs. Zhou et al. [27] introduced a configuration optimization model and innovatively proposed an optimization strategy where deviation satisfaction is considered in the objective function. The optimization interval of the strategy was selected through the sensitivity analysis of different preferences. Dong et al. [28] reported a refined modeling and coordinated configuration method for the electric-hydrogen-heat-gas-integrated energy system and hybrid energy storage system. They designed a co-optimal configuration model and concluded that the refined modeling could effectively reduce the cost and carbon emissions through case studies. The above work focuses on optimizing system architecture to enhance performance, rather than proposing a dispatch strategy, which undoubtedly represents a significant void.

1.3. Research gap and contribution

Based on a review of existing works, we have identified several research gaps in the operation of IHEUS in off-grid microgrids to reduce energy costs and improve system reliability. First, while most studies focus on hybrid energy storage systems incorporating batteries, few explore IHEUS configurations relying exclusively on hydrogen energy storage. Second, although the waste heat recovery potential of PEMEL and PEMFCs is well-documented [29,30], existing works often incorporate additional heat-producing equipment like gas boilers. Designing an IHEUS that efficiently recovers and utilizes waste heat is critical for practical implementation. Third, current research predominantly emphasizes single-objective dispatch optimization, neglecting the multi-objective trade-offs among hydrogen production, utilization, and waste heat recovery. Moreover, many studies neglect the impact of power fluctuations on the aging of hydrogen energy devices, and quantifying this aging is crucial for extending component life and improving IHEUS economics. To address these gaps, this study proposes an IHEUS framework integrating waste heat recovery and a life cycle-aware multi-objective dispatch optimization strategy. This paper attempts to address the above problems in the following steps:

1) This study designs an IHEUS structure that focuses on waste heat recovery and utilization, addressing the gap where existing studies often incorporate additional heat-producing equipment like gas boilers. By modeling the system according to thermodynamic principles, the study calculates the heat output characteristics of PEMEL and PEMFC and determines the heat generated during operation. This recovered waste heat is then reintegrated into the system to enhance its overall energy efficiency, making the approach more applicable in practical scenarios.
2) A multi-objective optimization model is constructed that considers both waste heat recovery and the life cycle of the system, filling the gap where previous research often overlooks the aging of hydrogen energy devices due to power fluctuations. The model includes the derivation and calculation of voltage degradation in PEMEL and PEMFC as a measure of aging, which is crucial for extending the life of system components. By incorporating these factors, the model optimizes the system for three key objectives: life cycle operating costs, overall energy efficiency, and the energy supply loss probability (ESLP).
3) To address the variability in typical operational conditions, the study uses clustering to identify four typical scenarios. It then applies the NSGA-III algorithm to solve the proposed multi-objective optimization problem under these scenarios. By determining the index weights and filtering out the optimal operation parameters through the entropy weighting method based on TOPSIS, the study identifies the optimal operation strategies. This approach not only enhances the economic operation of the system but also improves its efficiency and stability across different environmental conditions, thus filling a significant gap in the current research.

The rest of this paper is structured as follows. Section 2 first develops the performance model of IHEUS and the aging model of key devices. A multi-objective optimization model considering waste heat recovery and life cycle cost is established with corresponding operational constraints. Next, a solving strategy is reported using NSGA-III joint entropy weight TOPSIS. Section 3 verifies the advantages of the developed model and analyzes the simulation results corresponding to the relevant metrics. The conclusions are given in Section 4.

2. Methodology

The proposed structure of off-grid IHEUS is shown in Fig. 1. The IHEUS mainly consists of a PEMEL, a PEMFC, hydrogen storage tanks (HST), a hydrogen refueling station (HRS), and a heat storage tank (HT). The system utilizes the structure of a DC microgrid to deliver hydrogen-generated electricity directly to the load, enabling efficient energy utilization. In addition, through the electrical-thermal coupling characteristics of PEMEL and PEMFC, not only does the system involve the electrochemical reactions of hydrogen production and power generation, but it also recovers the waste heat generated in the energy conversion process. The centralized heat recovery is carried out through the cooling water circulation line, realizing the secondary utilization of by-product heat. By coordinating the work between the devices and taking advantage of the multi-energy complementarity of hydrogen energy, the joint production and utilization of electricity, hydrogen, and heat are realized, thus improving the comprehensive energy efficiency and economic operation of the system. Additionally, the photovoltaic (PV) and wind turbine (WT) depicted in the figure are renewable energy

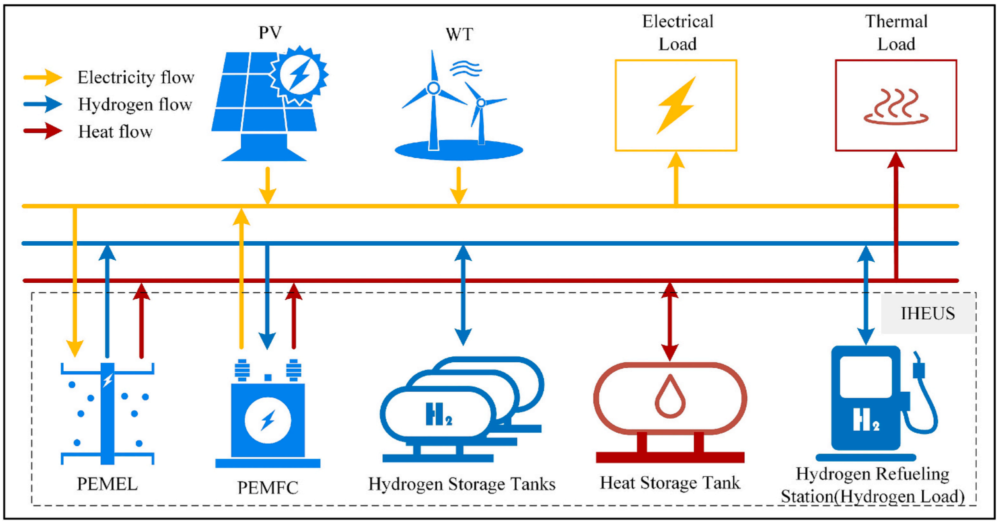

Fig. 1. System configuration of a microgrid with off-grid IHEUS.

generation devices, while the electrical load and thermal load represent the energy demands connected to the same microgrid. The models that describe the electrical, hydrogen, and thermal outputs of the key devices are developed as follows.

2.1. Model of system

The system involved in this study mainly consists of a renewable energy generation subsystem, a hydrogen energy subsystem, and an energy storage subsystem. The hydrogen energy subsystem, as the main participating system of energy conversion, needs to be described by an electric-hydrogen-thermal multiphysical coupling model.

2.1.1. Renewable energy power generation subsystem

Renewable energy sources mainly include wind and solar energy, and the corresponding power generation equipment involves wind turbines and photovoltaic panels.

1) Wind turbine

The real-time generation of a wind turbine mainly depends on the characteristics of the rotor and the wind speed at the hub height. The output power of the wind turbine at time t is given by [31]

$$P_{\mathrm{WT}}(t)=\begin{cases}0 & v(t)\le v_{\mathrm{in}}\text{or } v(t)\ge v_{\mathrm{out}}\\ P_r\cdot\dfrac{v(t)-v_{\mathrm{in}}}{v_r-v_{\mathrm{in}}} & v_{\mathrm{in}}\le v(t)\le v_r\\ P_r & v_r\le v(t)\le v_{\mathrm{out}}\end{cases}\tag{1}$$

where P_r is the rated power output of the wind turbine, and $v(t)$ is the wind speed at time t. v_r, v_{in}, and v_{out} represent the rated, cut-in, and cut-off wind speeds, respectively.

2) Photovoltaic panels

The generated photovoltaic (PV) power at time t is calculated by [32]

$$P_{\mathrm{PV}}(t)=W(t)A_{\mathrm{PV}}\eta_{\mathrm{PV}}(t)\tag{2}$$

where W is the solar irradiance, P_{PV} is the output power of the PV system, A_{PV} is the area of the PV panels, and η_{PV} is the power generation efficiency of the PV system.

2.1.2. Hydrogen energy subsystem

In this section, the mechanism model for both PEMEL and PEMFC, which comprises an electrochemical model and a thermodynamic model, will be derived. In this framework, thermal parameters—such as the temperature used in the electrochemical model—are calculated from the thermodynamic model to couple the device's electrothermal characteristics.

The hydrogen production/consumption of the PEMEL or PEMFC is only related to the current I:

$$n=\frac{I}{2F}\tag{3}$$

where n is the amount of generated hydrogen and F is Faraday's constant.

1) PEMEL

The cell voltage of PEMEL can be calculated by [33]

$$V_{\mathrm{el}}=E_{\mathrm{oc\_el}}+V_{\mathrm{act\_el}}+V_{\mathrm{con\_el}}+V_{\mathrm{ohm\_el}}\tag{4}$$

where

$$\begin{cases}E_{\mathrm{oc\_el}}=E_0+\dfrac{RT_{\mathrm{el}}}{2F}\left[\ln\left(p_{\mathrm{H_2\_el}}p_{\mathrm{O_2\_el}}^{0.5}\right)\right]\\ V_{\mathrm{act\_el}}=\dfrac{2RT_{\mathrm{el}}}{F}\left[\operatorname{arcsinh}\left(\dfrac{i}{2i_{0\_\mathrm{an}}}\right)+\operatorname{arcsinh}\left(\dfrac{i}{2i_{0\_\mathrm{ca}}}\right)\right]\\ V_{\mathrm{con\_el}}=-\dfrac{RT_{\mathrm{el}}}{nF}\ln\left(1-\dfrac{i}{i_{\max}}\right)\\ V_{\mathrm{ohm\_el}}=I_{\mathrm{el}}\cdot R_{\mathrm{ohm\_el}}\end{cases}\tag{5}$$

where $E_{\mathrm{oc\_el}}$, $V_{\mathrm{act\_el}}$, $V_{\mathrm{con\_el}}$ and $V_{\mathrm{ohm\_el}}$ are the open-circuit voltage, activation overvoltage, concentration difference overvoltage, and ohmic overvoltage of PEMEL, respectively. E_0 is the reference voltage, R is the gas constant, F is Faraday's constant, and T_{el} is the stack temperature. $I_{\mathrm{el}} = i\cdot A$ is the operating current, where i and A represent the current density and electrode cross-sectional area, respectively. Furthermore, i_{0_an} and i_{0_ca} represent the exchange current densities in the anode and cathode, respectively, $i_{\max}$ is a defined maximum current density, and $R_{\mathrm{ohm\_el}}$ is the PEMEL cell resistance.

The heat production of PEMEL can be calculated by

$$C_{s\_\mathrm{el}}\frac{dT}{dt}=E_{\mathrm{el}}+\sum(F_iH_i)_{\mathrm{in}}-\sum(F_iH_i)_{\mathrm{out}}-Q_{\mathrm{el}}\tag{6}$$

where C_{s_el} is the total heat capacity of the stack, E_{el} is the input energy of PEMEL, F_i and H_i represent the molar flow rate and molar enthalpy of substance i, respectively. Q_{el} is the heat exchange between the stack and the atmosphere/cooling circuit (Table 1).

2) PEMFC

The cell voltage of PEMFC can be calculated by [33]

$$V_{fc} = E_{oc\_fc} - V_{act\_fc} - V_{con\_fc} - V_{ohm\_fc} \tag{7}$$

$$\begin{cases} E_{oc\_fc} = \dfrac{\Delta G}{2F} + \dfrac{\Delta S}{2F}(T - T_{fc}) + \dfrac{RT_{fc}}{2F}\left[\ln\left(p_{H_2} p_{O_2}^{0.5}\right)\right] \\ V_{act\_fc} = \xi_1 + \xi_2 T_{fc} + \xi_3 T_{fc} \ln\left(\dfrac{p_{O_2}}{5.08 \times 10^6 \exp(-498/T_{fc})}\right) + \xi_4 T_{fc} \ln(I_{fc}) \\ V_{con\_fc} = b_1 \exp(b_2 I_{fc}) \\ V_{ohm\_fc} = I_{fc} \cdot R_{ohm\_fc} \end{cases} \tag{8}$$

where E_{oc_fc}, V_{act_fc}, V_{con_fc} and V_{ohm_fc} are the open-circuit voltage, activation overvoltage, concentration difference overvoltage, and ohmic overvoltage of PEMFC, respectively. ΔG is Gibbs free energy change, ΔS is entropy change, I_{fc} is the cell current, T is the reference temperature, T_{fc} is the cell temperature, and b_1 and b_2 are empirical coefficients fitted by experiments.

The heat production of PEMFC while operating can be calculated by the following formula:

$$C_{s\_fc} \frac{dT}{dt} = Q_{fc} = E_{tot\_fc} - E_{fc} - Q_{cool} - Q_{loss} \tag{9}$$

where Q_{fc} is the heat absorption power of the stack, and C_{s_fc} is the heat capacity. $E_{tot\_fc} = \int_0^t (n_{fc} \times \text{LHV})dt$ is the total power entering the stack, $E_{fc} = \int_0^t (V_{fc} I_{fc})dt$ is the power produced by PEMFC, and Q_{cool} and Q_{loss} are the heat taken away by cooling water and radiated outward by the stack, respectively (Table 2).

2.1.3. Energy storage subsystem

The energy in the system is stored in HST and HT in the form of hydrogen energy and thermal energy, respectively.

1) HST

HST absorbs hydrogen produced by PEMEL and it also supplies hydrogen to the PEMFC and HRS. The state of hydrogen (SOH) is used to describe how much HST is stored, calculated by

$$\text{SOH}_{\text{HST}}(t) = \text{SOH}_{\text{HST\_0}} + \left[\frac{1}{M_{H_2}} \int_0^t \left(\underbrace{F_{H_2,el}}_{\text{Output } H_2 \text{ molar flow of PEMEL}} - \underbrace{F_{H_2,fc}}_{\text{Input } H_2 \text{ molar flow of PEMFC}} - \underbrace{F_{H_2,\text{HRS}}}_{\text{Input } H_2 \text{ molar flow of HRS}} \right) dt \right] \Big/ \text{SOH}_{\text{HST\_max}} \tag{10}$$

Table 2
Values of parameters in PEMFC.

Parameter	Value	Parameter	Value
ξ_1	-0.9514	b_1	3×10^{-5} (V)
ξ_2	0.00312	b_2	8×10^{-3} (cm^2/mA)
ξ_3	7.4×10^{-5}	C_{s_fc}	135.1 (kJ/K)
ξ_4	-1.87×10^{-4}		

where $\text{SOH}_{\text{HST\_0}}$ is the initial hydrogen mass, M_{H_2} is the molar mass of the hydrogen, and $\text{SOH}_{\text{HST\_max}}$ is the maximum capacity of HST. The input and output hydrogen flow rates of the HST are calculated based on the PEMEL model, the PEMFC model, and the demand for hydrogen automobiles.

2) HT

HT stores the waste heat recovered from PEMEL and PEMFC and supplies it to the thermal load. The state of HT can be calculated by

$$Cap_{\text{HT}}(t) = Cap_{\text{HT\_0}} + \left[\int_0^t \left(\underbrace{Q_{el}}_{\text{Heat recycled by PEMEL}} + \underbrace{Q_{fc}}_{\text{Heat recycled by PEMFC}} - \underbrace{Q_{\text{TL}}}_{\text{Heat supplied to TL}} \right) dt \right] \Big/ Cap_{\text{HT\_max}} \tag{11}$$

where $Cap_{\text{HT\_0}}$ is the initial heat storage, and $Cap_{\text{HT\_max}}$ is the maximum capacity of HT. The input and output heat of HT are calculated based on the PEMEL model, the PEMFC model, and the thermal load.

At this point, the models of the key devices have been derived, based on which a multi-objective optimization model will be derived next.

2.2. Multi-objective optimization model

The established mechanism models of each device delineate the interplay of multiple energy flows within the system. Moreover, achieving economic operation requires considering both maintenance costs and the expenses associated with replacing aged devices during operation. For instance, in industrial systems, predictive maintenance and other cost factors have limited impact on short-term operational strategies. Instead, these costs become more relevant for long-term planning and total life-cycle cost analysis, where the emphasis shifts towards overall system sustainability rather than immediate operational efficiency [34]. Hence, we propose an operational target that incorporates life cycle costs. However, solely prioritizing economic operation may inadvertently constrain device operating conditions, potentially compromising system energy efficiency and supply stability. To address this, we introduce two objectives: comprehensive system energy efficiency and energy supply loss probability (ESLP), ensuring both energy demand satisfaction and enhanced economic operation

Table 1
Values of parameters in PEMEL.

Parameter	Value	Parameter	Value
i_{0_an}	2×10^{-7} (A/cm^2)	i_{max}	2 (A/cm^2)
i_{0_ca}	2×10^{-3} (A/cm^2)	C_{s_el}	61.9 (kJ/K)

capability. In light of these objectives, our study formulates a multi-objective optimization model that accounts for life cycle operating costs, comprehensive energy efficiency, and ESLP of IHEUS. Given that the operational state of PEMEL and PEMFC significantly influences aging and comprehensive energy efficiency, the power ceiling of PEMFC and the maximum hot water flow rate of HT (i.e., the heat release ceiling) determine energy supply loss probability. Consequently, the variables subject to optimization in our model encompass the power upper limits of PEMEL and PEMFC, as well as the heat release upper limit of HT.

2.2.1. Degradation of devices

PEMEL degradation can lead to an increase in operating voltage, with dynamic operations being the primary contributor to degradation across its components. Studies have suggested that the voltage degradation of PEMEL varies across different operational conditions, and ΔV_{el} serves as a quantitative measure to characterize PEMEL aging. ΔV_{el} is calculated by [35]

$$\Delta V_{\mathrm{el}} = N_{\mathrm{el}} \cdot \left(t_{\mathrm{el}\_m} \cdot V_{\mathrm{el}\_m} + t_{\mathrm{el}\_l} \cdot V_{\mathrm{el}\_l} + t_{\mathrm{el}\_h} \cdot V_{\mathrm{el}\_h} + t_{\mathrm{el}\_r} \cdot V_{\mathrm{el}\_r}\right) \tag{12}$$

where N_{el} is the number of PEMEL cells, and t_{el_m}, t_{el_l}, t_{el_h}, and t_{el_r} are the operating times under the corresponding operating conditions, respectively. V is the degree of voltage degradation for each operating condition, as shown in Table 3.

Like PEMEL, PEMFC also causes voltage degradation due to dynamic operating conditions. The voltage degradation ΔV_{fc} of PEMFC can be calculated by the following formula [36]

$$\Delta V_{fc} = N_{fc} \cdot \left(t_{fc\_m} \cdot V_{fc\_m} + t_{fc\_l} \cdot V_{fc\_l} + t_{fc\_h} \cdot V_{fc\_h} + t_{fc\_r} \cdot V_{fc\_r}\right) \tag{13}$$

where N_{fc} is the number of PEMFC cells, and t_{fc_m}, t_{fc_l}, t_{fc_h}, and t_{fc_r} are the operating times under the corresponding operating conditions, respectively. V is the degree of voltage degradation for each operating condition, as shown in Table 2.

The aging process of devices such as electrolyzers and fuel cells is influenced by various factors, including ambient temperature, humidity, and start-stop frequency; however, the primary manifestation of these factors' impact on device aging is voltage degradation [37]. In addition to the quantified electrochemical aging mentioned above, mechanical aging of PEMEL and PEMFC can also lead to a decline in device efficiency. However, existing studies indicate that the impact of mechanical aging on device efficiency is far less significant than that of electrochemical aging. Moreover, mechanical aging can be greatly delayed or even suppressed through improvements in structure and materials. For example, Lyu et al. [38] replaced the iridium catalyst in the device with IrO2 ink, and experiments showed that IrO_2 ink remained stable throughout the experimental period, did not affect the reaction on the PEMEL electrode, and significantly reduced damage to the membrane electrode assembly (MEA) compared to traditional iridium catalysts. Zhou et al. [39] explored the impact of bubble accumulation on PEMEL performance and suggested that altering the porous transport layer (PTL) and flow channel structure could effectively promote bubble transport, thereby preventing large bubble accumulation and extending the electrolyzer's lifespan. Huang et al. [40] proposed a theoretical leakage prediction model that discussed the quantitative impact of mechanical factors, environment, and geometry on the sealing performance of compressed seals. They suggested that reducing surface roughness and gasket thickness could mitigate stress loss effects on leakage rates, and that optimizing design parameters could significantly alleviate stress relaxation effects in sealing structures during long-term operation, thereby enhancing sealing performance. Zhao et al. [41] conducted a 150-h test on fuel cells and found that the early rapid performance degradation of the stack was due to a reduction in catalyst active surface area and increased hydrogen penetration. They concluded that optimizing the catalyst layer process and membrane materials could effectively maintain stable fuel cell performance. In summary, the impact of mechanical aging on device performance can be avoided at the design stage, so it is not considered in this paper's model (Table 4).

Table 3
Voltage degradation under dynamic conditions of PEMEL.

Operating conditions	Parameters	Power range (kW)	Voltage degradation (μV/h)
Maintaining operation	V_{el_m}	10	1.5
Low power fluctuation operation	V_{el_l}	(10,120)	50
High power fluctuation operation	V_{el_h}	(120,200)	66
Constant rated power operation	V_{el_r}	200	196

Table 4
Voltage degradation under dynamic conditions of PEMFC.

Operating conditions	Parameters	Power range (kW)	Voltage degradation (μV/h)
Maintaining operation	V_{fc_m}	3	27
Low power fluctuation operation	V_{fc_l}	(3,80)	8.622
High power fluctuation operation	V_{fc_h}	(80,120)	10
Constant rated power operation	V_{fc_r}	120	126

2.2.2. Life cycle cost

The optimal operation planning in this study aims to achieve economically viable and stable operation of the existing IHEUS, with a primary focus on operational efficiency rather than initial construction costs. Consequently, only operation and maintenance costs, degradation costs, and replacement costs are considered. Notably, the degradation and replacement costs are directly correlated with the equipment aging mechanisms discussed in the preceding subsection, collectively constituting a significant proportion of the total operational expenditures. Given the system's operation in off-grid conditions, it is imperative to establish an evaluation framework that comprehensively aligns with the operational demands of renewable energy systems. Accordingly, the objective function—incorporating the lifecycle cost of IHEUS—is formulated as follows:

$$C_{sys} = C_{o\&m} + C_{deg} + C_{rep} + C_{\mathrm{H}_2} \tag{14}$$

where $C_{o\&m}$ and C_{deg} are related to the initial investment cost of building the system, C_{inv}, which is expressed as follows

$$C_{inv} = C_{\mathrm{WT}} + C_{\mathrm{PV}} + C_{\mathrm{el}} + C_{\mathrm{fc}} + C_{\mathrm{HST}} + C_{\mathrm{HT}} \tag{15}$$

where C_{i} is the total investment cost of each component of IHEUS, and the formula is expressed as follows

$$\begin{cases} C_{\mathrm{WT}} = P_{\mathrm{WT}} \cdot C_{\mathrm{WT},0} \\ C_{\mathrm{PV}} = P_{\mathrm{PV}} \cdot C_{\mathrm{PV},0} \\ C_{\mathrm{el}} = P_{\mathrm{el}} \cdot C_{\mathrm{el},0} \\ C_{\mathrm{fc}} = P_{\mathrm{fc}} \cdot C_{\mathrm{fc},0} \\ C_{\mathrm{HST}} = V_{\mathrm{HST}} \cdot C_{\mathrm{HST},0} \\ C_{\mathrm{HT}} = Cap_{\mathrm{HT}} \cdot C_{\mathrm{HT},0} \end{cases} \tag{16}$$

Table 5
The values of the relevant parameters of the objective function.

Parameters	Value	Parameters	Value
$C_{\mathrm{WT},0}$ (￥/kW)	15,000	χ_{HT}	0.4
$C_{\mathrm{PV},0}$ (￥/kW)	7000	ψ_{trade}(￥/Nm^3)	3
$C_{el,0}$ (￥/kW)	9000	$\mathrm{SOH}_{\mathrm{HST\_min}}$	10%
$C_{fc,0}$ (￥/kW)	10,000	$\mathrm{SOH}_{\mathrm{HST\_max}}$	90%
$C_{\mathrm{HST},0}$ (￥/Nm^3)	295.5	$\mathrm{SOH}_{\mathrm{HT\_min}}$	20%
$C_{\mathrm{HT},0}$ (￥/kWh)	1500	$\mathrm{SOH}_{\mathrm{HT\_max}}$	80%

where $C_{i,0}$ is the unit price of each component and its value is shown in Table 5. P_{WT}, P_{PV}, P_{el}, and P_{fc} are the rated power of the WT, PV, PEMEL, and PEMFC, V_{HST} is the maximum capacity of the HST, and Cap_{HT} is the maximum capacity of the HT. The annual O&M costs can be approximated by the initial construction costs:

$$C_{o\&m} = C_{o\&m\_PV} + C_{o\&m\_WT} + C_{o\&m\_el} + C_{o\&m\_fc} + C_{o\&m\_HST} \tag{17}$$

$$\begin{cases} C_{o\&m\_WT/PV} = \alpha_{WT/PV} \times C_{WT/PV} \\ C_{o\&m\_el/fc} = \beta_{el/fc} \times C_{el/fc} \\ C_{o\&m\_HST/HT} = \gamma_{HST/HT} \times C_{HST/HT} \end{cases} \tag{18}$$

where $\alpha_{WT/PV}$ is the operation and maintenance cost coefficient of WT and PV, $\beta_{el/fc}$ is the operation and maintenance cost coefficient of PEMEL and PEMFC, $\gamma_{HST/HT}$ is the operation and maintenance cost coefficient of HST and HT, $\alpha_{WT/PV}$, $\beta_{el/fc}$, and $\gamma_{HST/HT}$ are 3%, 4%, and 0.5% respectively in this paper.

During operation, the degradation of PEMEL and PEMFC will directly affect the life of each device. Therefore, the degradation costs of PEMEL and PEMFC need to be considered.

$$C_{deg} = C_{deg\_el} + C_{deg\_fc} \tag{19}$$

$$\begin{cases} C_{deg\_el} = \dfrac{\Delta V_{el}}{V_{eol\_el}} \cdot C_{el} \\ C_{deg\_fc} = \dfrac{\Delta V_{fc}}{V_{eol\_fc}} \cdot C_{fc} \end{cases} \tag{20}$$

where V_{eol_el} and V_{eol_fc} are the voltage of the PEMEL and PEMFC when they need to be replaced. In this study, V_{eol_el} was set to be 20% of the rated voltage of the PEMEL, and V_{eol_fc} was set to be 10% of the rated voltage of the PEMFC.

When the degradation of the PEMEL and PEMFC reaches a certain level, these devices necessitate replacement. However, relying solely on expert judgment to set a fixed replacement period may lead to premature replacement before the device reaches its abandonment threshold or excessive aging, resulting in significant efficiency degradation. To address this, a replacement cost function is devised to precisely determine if the device meets the replacement criteria. The number of replacements hinges on whether the device reaches its end of life (EOL) within the designated IHEUS design life. The replacement cost function is outlined as follows:

$$C_{rep} = C_{rep\_el} + C_{rep\_fc} \tag{21}$$

$$\begin{cases} C_{rep\_el} = \dfrac{N_{life} \cdot \Delta V_{el}}{V_{eol\_el}} \cdot C_{el} - 1 \\ C_{rep\_fc} = \dfrac{N_{life} \cdot \Delta V_{fc}}{V_{eol\_fc}} \cdot C_{fc} - 1 \end{cases} \tag{22}$$

where N_{life} designed a lifetime for IHEUS, which in this study was 20 years.

In addition, IHEUS will sell hydrogen to HRS. The hydrogen selling cost function is

$$C_{H_2} = \left(\mathrm{SOH}_{ini} - \mathrm{SOH}_{fin}\right) V_{HST} \psi_{trade} \tag{23}$$

where SOH_{ini} is the initial SOH of HST, SOH_{fin} is the year-end reserves of HST, and ψ_{trade} is the trade cost coefficient per Nm^3.

2.2.3. Energy efficiency

The average comprehensive energy utilization efficiency of the PEMEL and PEMFC is calculated as:

$$\begin{cases} \eta_{tot\_el} = \dfrac{\mathrm{LHV} \cdot \int_0^t n_{H_2\_el}(t)dt + Q_{re\_el}}{\int_0^t P_{el}(t)dt} \times 100\% \\ \eta_{tot\_fc} = \dfrac{\int_0^t P_{fc}(t)dt + Q_{re\_fc}}{\mathrm{LHV} \cdot \int_0^t n_{H_2\_fc}(t)dt} \times 100\% \end{cases} \tag{24}$$

where LHV is the low heating value of hydrogen with a value of 242 kJ/mol. $n_{H_2_el}(t)$represents the amount of hydrogen produced by the PEMEL at the time t, and $n_{H_2\_fc}(t)$ represents the amount of hydrogen consumed by the PEMFC at the time t. Q_{re_el} and Q_{re_fc} are the heat recovered by the PEMEL and the PEMFC, respectively. $P_{el}(t)$ is the power consumed by the PEMEL at time t, and $P_{fc}(t)$ is the power emitted by the PEMFC at the time t. Then the expression for the calculation of the integrated energy efficiency of the system is as follows:

$$\eta_{tot\_sys} = \eta_{tot\_el} \cdot \eta_{tot\_fc} \tag{25}$$

2.2.4. Energy supply loss probability

In system design, it's common practice to set a large system capacity to ensure stability. However, such a design often incurs excessive construction costs. To examine the relationship between system capacity and construction cost, we make the following assumptions: the annual electrical load demand is 120 kW, the PEMFC rated power is 120 kW, the maximum PEMFC output power allowed in scenario 1 is 120 kW, and in scenario 2, it's 110 kW. Using the calculation formula for equipment aging degree and operation cost as outlined in Sections 2.2.1 and 2.2.2, we compute the aging cost for both schemes and plot the results in Fig. 2.

From the analysis in Section 2.2.1, it can be concluded that since fuel cells experience the most severe aging when operating at rated power, running them at slightly lower power can significantly slow down the aging process while avoiding excessive energy shortages. It's evident that permitting some supply shortages during operation can notably diminish the economic input of the system. In this context, Yazdani [42] introduced the power supply loss probability index, which denotes the fraction of system capacity shortage in a year. However, in this study, considering the inclusion of heating loss in addition to power supply, this index is revised to the energy supply loss probability (ESLP). ESLP quantifies the proportion of total energy demand unmet by the system within a certain period relative to the total energy demand, expressed as:

$$\mathrm{ESLP} = \frac{\int_0^t E_{lack}(t)dt}{\int_0^t E_{demand}(t)dt} \times 100\% \tag{26}$$

where $E_{lack}(t)$ represents the energy that is in short supply at time t and $E_{demand}(t)$ represents the energy that is demanded at time t.

2.3. Constraints

Before determining the system operation constraints, the operation strategy of this system should be formulated first. According to the electrical/hydrogen/thermal characteristics of the device and the

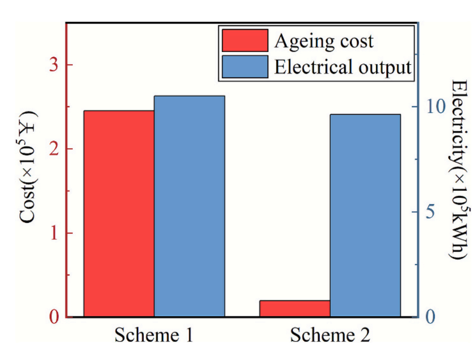

Fig. 2. Comparison of calculation results.

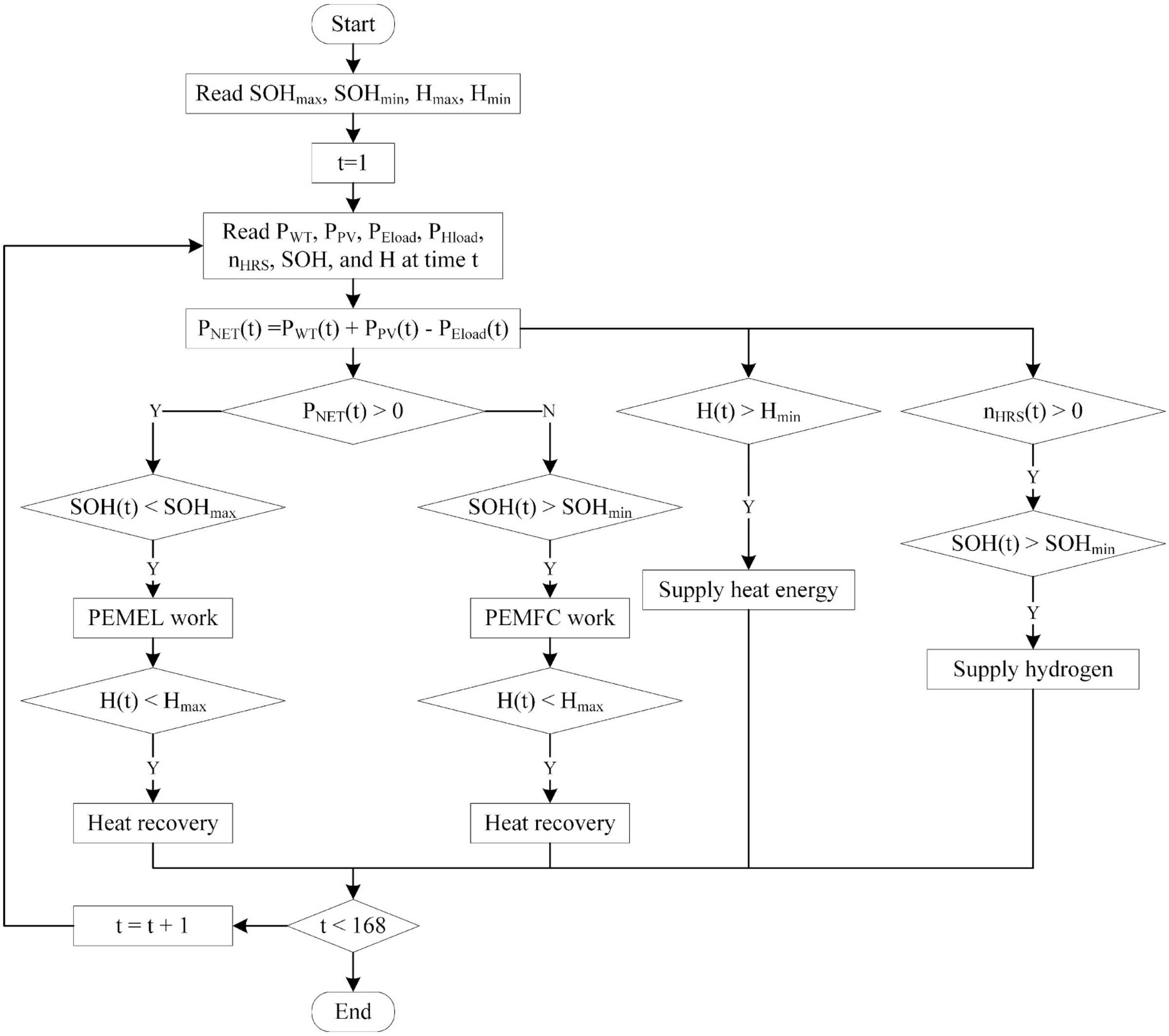

Fig. 3. Operation strategy flow chart.

objective function proposed in the previous section, the designed IHEUS operation strategy is shown in Fig. 3. In the figure, SOH_{max}, SOH_{min}, H_{max}, and H_{min} represent the upper and lower limits of HST and HT, respectively.

As depicted in the figure, electric energy generated by PV and WT is primarily allocated to fulfill the electrical load requirements. Any surplus electric energy is directed towards the PEMEL, where it is converted into hydrogen energy and stored in the HST. Should power demand exceed generation capacity, the PEMFC draws hydrogen from the HST to generate electricity, bridging the gap in the microgrid's power supply. Furthermore, the HST serves not only as a storage facility for hydrogen produced by the PEMEL and needed for the PEMFC but also as a hydrogen source for the HRS. Concurrently, while the PEMEL and PEMFC are operational, the heat recovery system captures waste heat from both systems, storing it in the HT to meet thermal load demands. These operations lay the foundation for the subsequent determination of corresponding operating constraints.

2.3.1. Energy balance constraints

During operation, the energy constraint of the system can be expressed as

$$\sum_{g\in G_i} P_g(t) + \sum_{k\in N_i} P_{ik}(t) = P_{el,i}(t) + P_{\mathrm{Load},i}(t) + x_i(t) \tag{27}$$

$$H_{\mathrm{el}}(t) + H_{\mathrm{fc}}(t) = H_{\mathrm{TL}}(t) + H_{\mathrm{HT}}(t) + y(t) \tag{28}$$

$$n_{\mathrm{H_2\_fc}}(t) + n_{\mathrm{H_2\_RHS}}(t) + n_{\mathrm{H_2\_HST}}(t) = n_{\mathrm{H_2\_el}}(t) \tag{29}$$

where Eq. (27) is the electric power constraint of the system. G_i represents the generation units at node i, including PV, WT, and PEMFC. N_i denotes the set of nodes directly connected to node i. represents the transmission power from node i to node k, with an upper limit of 65 kW set in this study. $P_{\mathrm{el},i}(t)$, and $P_{\mathrm{Load},i}(t)$ represent the electrical power consumed by PEMEL and electrical load at time t and node i, respectively. Eq. (28) is the heat power constraint. $H_{\mathrm{el}}(t)$ and $H_{\mathrm{fc}}(t)$ are the waste heat recovered from the PEMEL and PEMFC, respectively. H_{TL}(t) is the heat demand at time t, and $H_{\mathrm{HT}}(t)$ is the heat power stored/released by the HT at time t. In Eqs. (27) and (28), $x(t)$ and $y(t)$ represent the virtual supplement quantities when there is a supply-demand mismatch in the microgrid at time t. When they are non-zero, it indicates an energy supply shortage. Eq. (29) is the hydrogen exchange constraint. Where $n_{\mathrm{H_2\_fc}}(t)$ and $n_{\mathrm{H_2\_HRS}}(t)$ are the amount of hydrogen consumed by the PEMEL and the HRS, respectively, at time t. $n_{\mathrm{H_2\_HST}}(t)$ is the amount of hydrogen stored/released by the HST at time t, $n_{\mathrm{H_2\_el}}(t)$ is the amount of hydrogen produced by the PEMEL at time t.

2.3.2. Design and operating constraints

For IHEUS, the electric power depends on the working state of each device. Therefore, the power constraint of IHEUS is given by

$$\begin{cases} 0 \le P_{\mathrm{WT}}(t) \le P_{\mathrm{WT}} \\ 0 \le P_{\mathrm{PV}}(t) \le P_{\mathrm{PV}} \\ 0 \le P_{\mathrm{el}}(t) \le P_{\mathrm{el}} \\ 0 \le P_{\mathrm{fc}}(t) \le P_{\mathrm{fc}} \end{cases} \tag{30}$$

where P_{WT}, P_{PV}, P_{el}, and P_{fc} are the rated power of the WT, PV, PEMEL, and PEMFC.

The heat generation of the waste heat recovery system is contingent upon its operational status and the permissible thermal power of the thermal bus. Consequently, the thermal constraint of the system is outlined as follows:

$$\begin{cases} 0 \le H_{\mathrm{el}}(t) \le H_{\mathrm{el\_max}}(t) \\ 0 \le H_{\mathrm{fc}}(t) \le H_{\mathrm{fc\_max}}(t) \\ -\chi_{\mathrm{HT}} \cdot Cap_{\mathrm{HT\_max}} \le H_{\mathrm{HT}}(t) \le \chi_{\mathrm{HT}} \cdot Cap_{\mathrm{HT\_max}} \end{cases} \tag{31}$$

where $H_{\mathrm{el\_max}}(t)$ and $H_{\mathrm{fc\_max}}(t)$ are the maximum heat power of the PEMEL and the PEMFC. $Cap_{\mathrm{HT\_max}}$ is the capacity of the HT, and χ_{HT} is the power coefficient of the HT.

For the energy storage subsystem, upper and lower limits are established for capacity. Hence, the capacity constraint of the energy storage unit is defined as:

$$\begin{cases} \mathrm{SOH}_{\mathrm{HST\_min}} \le \mathrm{SOH}_{\mathrm{HST}}(t) \le \mathrm{SOH}_{\mathrm{HST\_max}} \\ Cap_{\mathrm{HT\_min}} \le Cap_{\mathrm{HT}}(t) \le Cap_{\mathrm{HT\_max}} \end{cases} \tag{32}$$

where $\mathrm{SOH}_{\mathrm{HST\_max}}$ and $\mathrm{SOH}_{\mathrm{HST\_min}}$ represent the maximum and minimum state of hydrogen in the HST, and $Cap_{\mathrm{HT\_max}}$ and $Cap_{\mathrm{HT\_min}}$ represent the maximum and minimum capacity of the HT.

The values of the variables appearing in the objective function and constraints are shown in Table 5 [36].

2.4. Solution method

Multi-objective optimization problem (MOOP) is usually to find a compromise between several conflicting objectives, offering crucial guidance for practical engineering applications. The process of finding solutions to such problems is termed multi-objective optimization (MOO). In this study, the MOOP comprises three decision variables and three objective functions, expressed as:

$$Minimize\, y = f(x) = [C(x)\,, 1 - \eta(x)\,, \mathrm{ESLP}(x)\,] \tag{33}$$

where,

$$x = (P_{el\_\max}, P_{fc\_\max}, H_{\mathrm{TL\_max}}) \tag{34}$$

where P is the maximum power of PEMEL and PEMFC, and H is the maximum demand of TL, which are both in kW.

This MOOP needs to solve the three decision variables simultaneously to optimize the three objective functions. Furthermore, to improve the reliability of the solution set, it needs to search every part of the search space as far as possible. Therefore, this study uses NSGA to compute the Pareto front. However, NSGA does not clarify the importance of each objective function in the optimization process, and an objective weight determination method is needed to rank each solution in the Pareto front. Therefore, the TOPSIS based on the entropy weight method is used to obtain the optimal solution, ultimately yielding the final IHEUS dispatch optimization result.

2.4.1. Non-dominated sorting genetic algorithm III

In the existing studies, MOO mostly adopts NSGA to obtain the Pareto front. Compared to alternative optimization algorithms such as the Particle Swarm Optimization (PSO) algorithm and Deep Learning (DL) algorithm, NSGA stands out as a group search algorithm that optimizes multiple objective functions simultaneously by maintaining a set of non-dominated solutions [43]. This characteristic makes NSGA particularly suitable for addressing multi-objective optimization problems, and brings faster solving speed. Furthermore, PSO and DL algorithms tend to focus on local search, whereas MOOP often encompasses multiple local optimal solutions. NSGA, on the other hand, conducts a more comprehensive exploration of the solution space. Additionally, the dispatch optimization problem is often the optimization of multiple related objective functions. PSO is more suitable for parameter optimization in continuous space [44], and DL is more suitable for data recognition problems with large scale [45]. Therefore, NSGA is the best choice to solve MOOP in this study. Compared with the common NSGA-II, for the MOOP designed in this study, NSGA-III has better convergence and population diversity in high dimensions [46], so this study chooses NSGA-III to solve the designed MOOP.

For the MOOP designed in this study, the specific steps of NSGA-III are as follows:

1) Initialize the population: randomly generate the initial population, in which each individual contains a set of decision variables $P_{el\_\max}$, $P_{fc\_\max}$, and $H_{TL\_\max}$ values;
2) Fitness evaluation: For each individual in the population, calculate its corresponding objective function value $C(x)$, $\eta(x)$, and ESLP(x);
3) Non-dominated sorting: The individuals in the population are non-dominated sorted, and the individuals are divided into different levels, where the first level contains non-dominated solutions, the second level contains solutions that are dominated but do not dominate other solutions, and so on;
4) Calculate crowding distance: For each individual in each level, calculate its crowding distance;
5) Environmental selection: according to the non-dominated sorting and crowding distance, a group of high-quality individuals are selected as the parents of the next generation population;
6) Crossover and mutation: Crossover and mutation operations are performed on the selected parent individuals to generate new offspring individuals;
7) Mixed population: parent individuals and offspring individuals are merged into a mixed population;
8) Selection of the next generation: the individual with the best fitness from the mixed population is selected as the next generation population;
9) Repeat iteration: Repeat steps 2) to 8) until the number of iterations reaches the upper limit.

2.4.2. TOPSIS based on entropy weight

After obtaining the Pareto front, where each solution represents the best compromise among its class, a decision-making method is required to rank the solutions and identify the optimal solution. Among multi-criteria decision-making methods, the technique for order of preference by similarity to ideal solution (TOPSIS) is commonly employed in engineering design problems [47,48]. TOPSIS based on entropy weight solves the subjective weighting bias under multi-objective coupling of equipment by dynamically quantifying target weights with information entropy, and its proximity ranking further improves the robustness of decision making. The basic steps of TOPSIS are as follows:

Step 1. Determine the ideal solution $Z^{+} = (z_1^{+}, z_2^{+}, \ldots, z_p^{+})$ and the negative ideal solution $Z^{-} = (z_1^{-}, z_2^{-}, \ldots, z_p^{-})$.

$$z_j^{+} = \begin{cases} \max\limits_{1 \le i \le m} (v_{ij}) & \text{if } f_j \in F_1 \\ \min\limits_{1 \le i \le m} (v_{ij}) & \text{if } f_j \in F_2 \end{cases} \tag{35}$$

$$z_j^{-} = \begin{cases} \max\limits_{1 \le i \le m} (v_{ij}) & \text{if } f_j \in F_1 \\ \min\limits_{1 \le i \le m} (v_{ij}) & \text{if } f_j \in F_2 \end{cases} \tag{36}$$

where v is the product of each solution and the corresponding weight, F_1

denotes the set of benefit objectives, F_2 denotes the set of cost objectives, and $1 \le j \le n$.

Step 2. The distance from each solution to Z^+ and Z^- is calculated as follows:

$$S_i^+ = \sqrt{\sum_{j=1}^{n} \left(v_{ij} - z_j^+\right)^2} \quad i = 1, 2, ..., m \tag{37}$$

$$S_i^- = \sqrt{\sum_{j=1}^{n} \left(v_{ij} - z_j^-\right)^2} \quad i = 1, 2, ..., m \tag{38}$$

Step 3. The approximation degree of each solution to the ideal solution is calculated using the following formula:

$$C_i = \frac{S_i^-}{S_i^+ + S_i^-} \quad i = 1, 2, ...m \tag{39}$$

In this case, a larger value of C_i indicates that this solution is better. In this study, determining the weights of each objective is challenging for the decision maker due to the intricate interrelations among operation cost, efficiency, and ESLP. Therefore, objective determination of these weights based on the characteristics of the data in the Pareto solution set is essential. The entropy weight method serves as an objective weighting method suited for this purpose [49]. Indeed, the entropy weight method relies solely on the intrinsic properties of the data, calculating the relative proximity of each optimal solution within the Pareto solution set. Subsequently, it selects the alternative with the highest relative proximity as the final optimal solution. The steps of TOPSIS based on entropy weight method are shown in Table 6.

In summary, when comparing the NSGA-II algorithm with the NSGA-III joint entropy weight TOPSIS method, the latter demonstrates significant advantages. First, NSGA-III excels in handling high-dimensional multi-objective optimization problems more effectively than NSGA-II, providing a more comprehensive and balanced set of non-dominated solutions in the objective space. Second, NSGA-III ensures diversity and uniform distribution of the solution set by introducing reference points, avoiding the issue of solution concentration in high-dimensional objectives that NSGA-II may encounter, thus enabling a more thorough exploration of the solution space. Additionally, the combination of NSGA-III with the entropy weight TOPSIS method further enhances optimization capabilities. While NSGA-III generates a diverse set of solutions, it cannot directly provide a single optimal solution, but the entropy weight TOPSIS method ranks the solutions by assigning relative importance weights to each objective, accurately selecting the optimal solution. Lastly, the NSGA-III joint entropy weight TOPSIS method shows stronger adaptability across different typical scenarios, effectively responding to scenario changes and identifying the optimal solution for each scenario, whereas NSGA-II might fall short when dealing with complex and variable scenarios. Therefore, the NSGA-III joint entropy weight TOPSIS method offers clear advantages over NSGA-II in terms of multi-objective optimization, solution set distribution, multi-scenario adaptability, and accuracy in selecting the optimal solution, making it particularly suitable for optimizing complex energy systems.

Table 6
Pseudo-code for TOPSIS based on entropy weight.

Algorithm 1 TOPSIS based on entropy weight
Input: $X_{mn} = [x_{ij}]$
Output: X_{op}
1: Indicator standardization: $\lambda_{ij} = \frac{x_{ij}}{\sqrt{\sum_{i=1}^{n} x_{ij}^2}}$
2: Determining weights: $O_j = -\frac{1}{\ln m}\sum_{i=1}^{m}\left(\frac{x_{ij}}{\sum_{i=1}^{m} x_{ij}^2}\ln\frac{x_{ij}}{\sum_{i=1}^{m} x_{ij}^2}\right)$
$W_j = -\frac{1 - O_j}{3 - \sum_{j=1}^{n} O_j}$
3: $v_{ij} = \lambda_{ij} W_{ij}$
4: Optimal and inferior solution calculation:
$z_j^+ = \begin{cases} \max_{1\le i\le m}(v_{ij}) & \text{if } f_j \in W_1 \\ \min_{1\le i\le m}(v_{ij}) & \text{if } f_j \in W_2 \end{cases}$
$z_j^- = \begin{cases} \max_{1\le i\le m}(v_{ij}) & \text{if } f_j \in F_1 \\ \min_{1\le i\le m}(v_{ij}) & \text{if } f_j \in F_2 \end{cases}$
5: Optimal and inferior solution distance calculation:
$S_i^+ = \sqrt{\sum_{j=1}^{n}\left(v_{ij} - z_j^+\right)^2} \quad i = 1, 2, ..., m$
$S_i^- = \sqrt{\sum_{j=1}^{n}\left(v_{ij} - z_j^-\right)^2} \quad i = 1, 2, ..., m$
6: Calculation of indicator scores: $C_i = \frac{S_i^-}{S_i^+ + S_i^-} \quad i = 1, 2, ...m$
7: Sort result output: $X_{op} = \{X_i \mid \max_{1\le i\le m}(C_i)\}$

2.5. Summary

This section details the multi-objective optimization dispatch scheme for IHEUS under off-grid condition. By establishing models of each device, the electricity, hydrogen, and heat output characteristics of the system are analyzed. Energy efficiency is improved by the utilization of waste heat recovery. Additionally, a comprehensive evaluation system is formed by quantifying the aging of the equipment, calculating the operation cost considering the life cycle, and combining it with the comprehensive energy efficiency and ESLP of the system. Finally, the NSGA-III joint entropy weight TOPSIS method was used to screen the optimization scheme and derive the optimal operation strategy. The detailed steps of optimizing the dispatch scheme are shown in Fig. 4.

3. Results and discussion

3.1. Case study

This study was conducted based on a demonstration project in Ningbo, China. Hydrogen energy systems, including PEMEL, PEMFC, and HST, are situated within the project, forming a standard IHEUS. Given the project's coastal location and abundant renewable resources, wind power generation is utilized for energy supply. Additionally, the IHEUS within the project must cater to thermal load demands (e.g., household water) and hydrogen requirements (e.g., hydrogen fuel cell vehicles). Considering the project's coastal setting, variable climatic conditions, and considerable distance from the main grid, it is imperative for the IHEUS to have robust off-grid operational capabilities. In summary, the demonstration project serves as a tangible manifestation of the IHEUS concept, enabling the project to achieve energy self-sufficiency even under complete off-grid conditions, thereby providing a practical foundation for subsequent optimization strategies. The specific structure of the demonstration project is shown in Fig. 5. The power/capacity limits of each device in the demonstration project are shown in Table 7.

This study takes this project as an example to collect local annual climate and thermal power demand data to illustrate the design process of IHEUS multi-objective optimal dispatch. For the collected scenery load data of the park throughout the year, the clustering is carried out according to the output characteristics to obtain four typical scenes. The scenery data and the thermal demand curve of electric hydrogen for typical scenes are shown in Fig. 6.

As depicted in Fig. 6, (a) shows the strong wind and strong solar climate condition, which is marked as scene 1. (b) shows the climate condition of weak wind and strong solar, which is marked as scene 2. Fig. 6(c) shows the climate condition of weak wind and solar, which is marked as scene 3. (d) shows the strong wind and weak solar climate condition, which is marked as scene 4. In these scenarios, the demand for heat and hydrogen undergoes periodic fluctuations throughout the

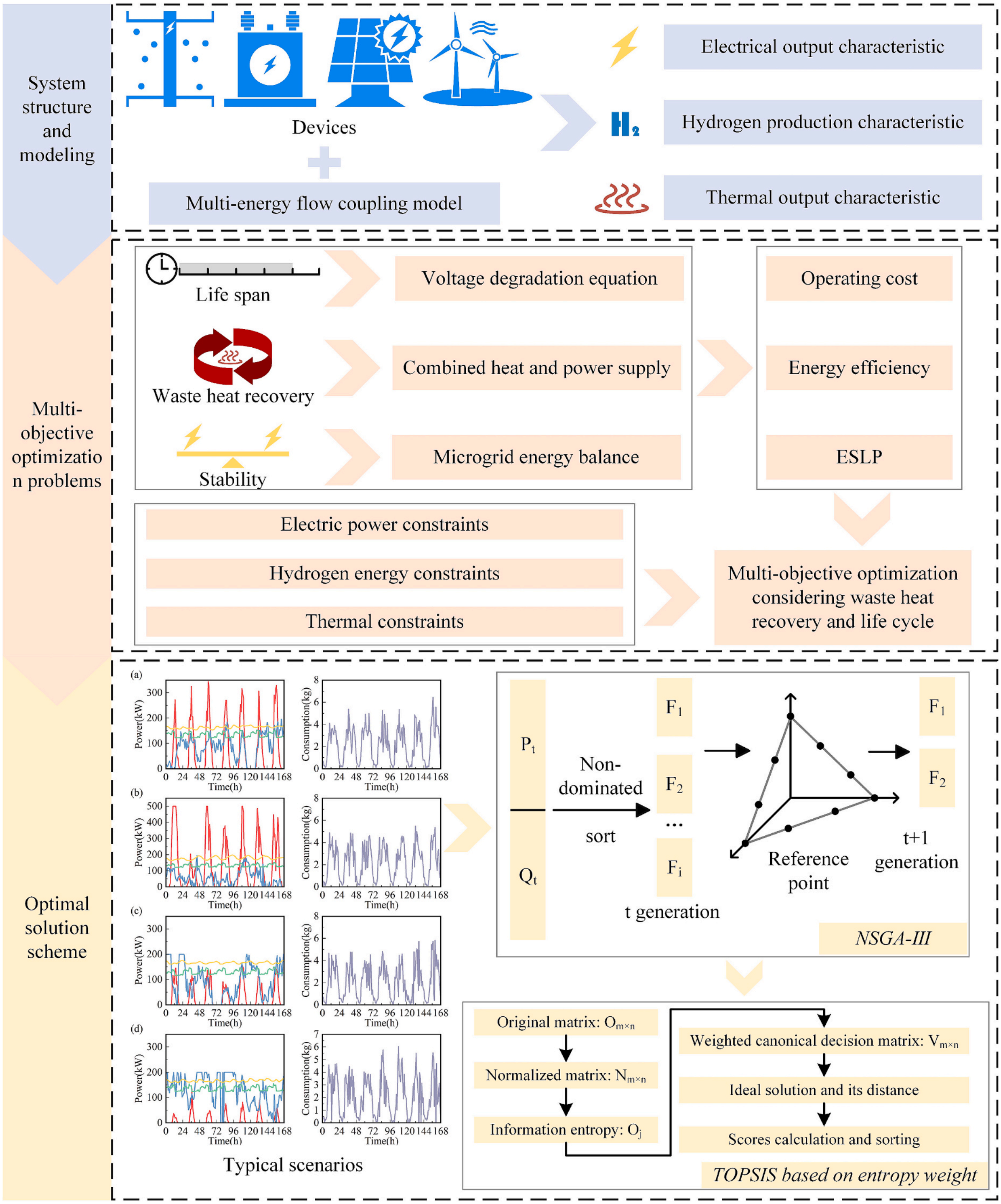

Fig. 4. Work frame of IHEUS multi-objective optimization dispatch scheme under off-grid conditions.

day, with lower demand during the morning and evening and higher demand during the day.

The following analysis focuses on the sensitivity of optimization parameters. This study employs Analysis of Variance (ANOVA) to examine the relationship between key parameters and optimization results. For the ANOVA, the clustering scenarios, electrolyzer power limit, and fuel cell power limit are chosen as the three parameters for IHEUS analysis. In this study, an L9 standard orthogonal array is used, and the results are presented in Tables 8, 9, and 10.

In one-way ANOVA, the F-value measures the impact of different factors on the target parameters. A larger F-value indicates a more significant effect of the factor on the target parameter, meaning that changes in this factor cause notable changes in performance. The contribution rate represents the extent to which a factor contributes to the total variation, with higher values indicating a greater influence on the response variable. From the table, it is evident that the scenario has the largest contribution rate to cost, efficiency, and ESLP. This indicates that different scenarios have the most significant impact on cost, efficiency, and ESLP, while the effects of P_{el} and P_{fc} are relatively smaller. However, within the same scenario, changes in P_{el} have a more pronounced effect on cost compared to P_{fc}. This is because the total construction cost of the electrolyzer is greater than that of the fuel cell, and

Fig. 5. Picture of the demonstration project.

Table 7
Capacity of the devices in the project.

Devices	Capacity	Devices	Capacity
WT	200 kW	PEMFC	120 kW*2
PV	500 kW	HST	5700Nm^3
PEMEL	200 kW*2	HT	3.6×10^6 kJ

operational costs are positively correlated with construction costs—the larger the construction cost, the greater its proportion of the total cost. Conversely, changes in P_{fc} have a more significant impact on system efficiency and ESLP compared to P_{el}, as the operating state of the fuel cell directly determines the stability of energy supply in IHEUS. In summary, in these three different variance analyses, the Scenario is the most influential factor in terms of cost, efficiency, and ESLP. Thus, dividing scenarios for dispatch optimization is crucial. The impacts of P_{el} and P_{fc} are relatively smaller but still vary within the same scenario, necessitating consideration of practical circumstances for optimal decision-making.

3.2. Optimization results

Based on the typical scene curves obtained through clustering in the preceding subsection, the multi-objective optimization of this research setting is conducted for various climate and demand conditions. The resulting Pareto front is depicted in Fig. 7.

In terms of the decision variable values depicted in Fig. 7(a), when the climate condition is scenario 1, the electrical load fluctuation is small, and the hydrogen demand fluctuation is large, the renewable energy generation is sufficient to meet the demand of most of the electrical load in the microgrid, so the working state of PEMFC is concentrated in the range below 40 kW. Since the PV power generation under this condition is in the upper middle level, and thus the overall net power generation is less, the working state of PEMEL is concentrated in the interval below 100 kW. With no additional constraints on the thermal load demand, the thermal load supply state is more evenly distributed between 155 kW and 180 kW.

As shown in Fig. 7(b), when the climate condition is scenario 2, the electrical load fluctuates greatly, and the hydrogen demand fluctuates greatly. At this time, renewable energy generation is sufficient to meet the demand of most of the electrical load in the microgrid, so the working state of PEMFC is concentrated in the range below 40 kW. Since the PV generation is at a high level under this condition, and thus the overall net power generation is more, the working state of PEMEL is concentrated between 100 kW and 200 kW. With no additional constraints on the thermal load demand, the thermal load supply state is more evenly distributed between 155 kW and 180 kW.

As shown in Fig. 7(c), when the climate condition is scenario 3, the electrical load fluctuation is small, and the hydrogen demand fluctuation is large, the renewable energy generation is not enough to meet the demand of the electrical load in the microgrid at this time, so the working state of PEMFC is concentrated between 40 kW and 80 kW. Since the power generation of both PV and WT is less in this condition, the working state of PEMEL is concentrated in the interval below 100 kW. With no additional constraints on the thermal load demand, the thermal load supply state is more evenly distributed between 155 kW and 180 kW.

As shown in Fig. 7(d), when the climate condition is scenario 4, the electrical load fluctuation is small, and the hydrogen demand is concentrated. At this time, renewable energy generation is not enough to meet the demand of the electrical load in the microgrid, so the working state of the PEMFC is concentrated between 40 kW and 120 kW. The working state of PEMEL is also concentrated in the interval below 60 kW due to the low power generation of PV and WT in this condition. With no additional constraints on the thermal load demand, the thermal load supply state is more evenly distributed between 155 kW and 180 kW.

In terms of the optimization value of the objective function, when calculating the cost, the life cycle cost occupies most of it. According to (12) and (13), the quantification of the aging process is calculated according to the working state. However, in the optimization results, the operating conditions of the PEMEL and PEMFC are predominantly constrained to high power fluctuation scenarios. Consequently, the aging of these two devices throughout the simulation cycle can be approximated as a piecewise function. This approximation results in multiple instances of identical costs in the cost optimization, even though the other objective functions differ. Examining the efficiency and ESLP objective functions reveals a noticeable restrictive relationship between them. This is because the maximum efficiency operating point of both PEMFC and PEMEL occurs at lower power, and when PEMFC and PEMEL work at low power, the power generation, hydrogen production, and heat recovery are less, and the possibility of missing energy supply is greater. Therefore, as the system efficiency improves, the ESLP also tends to increase.

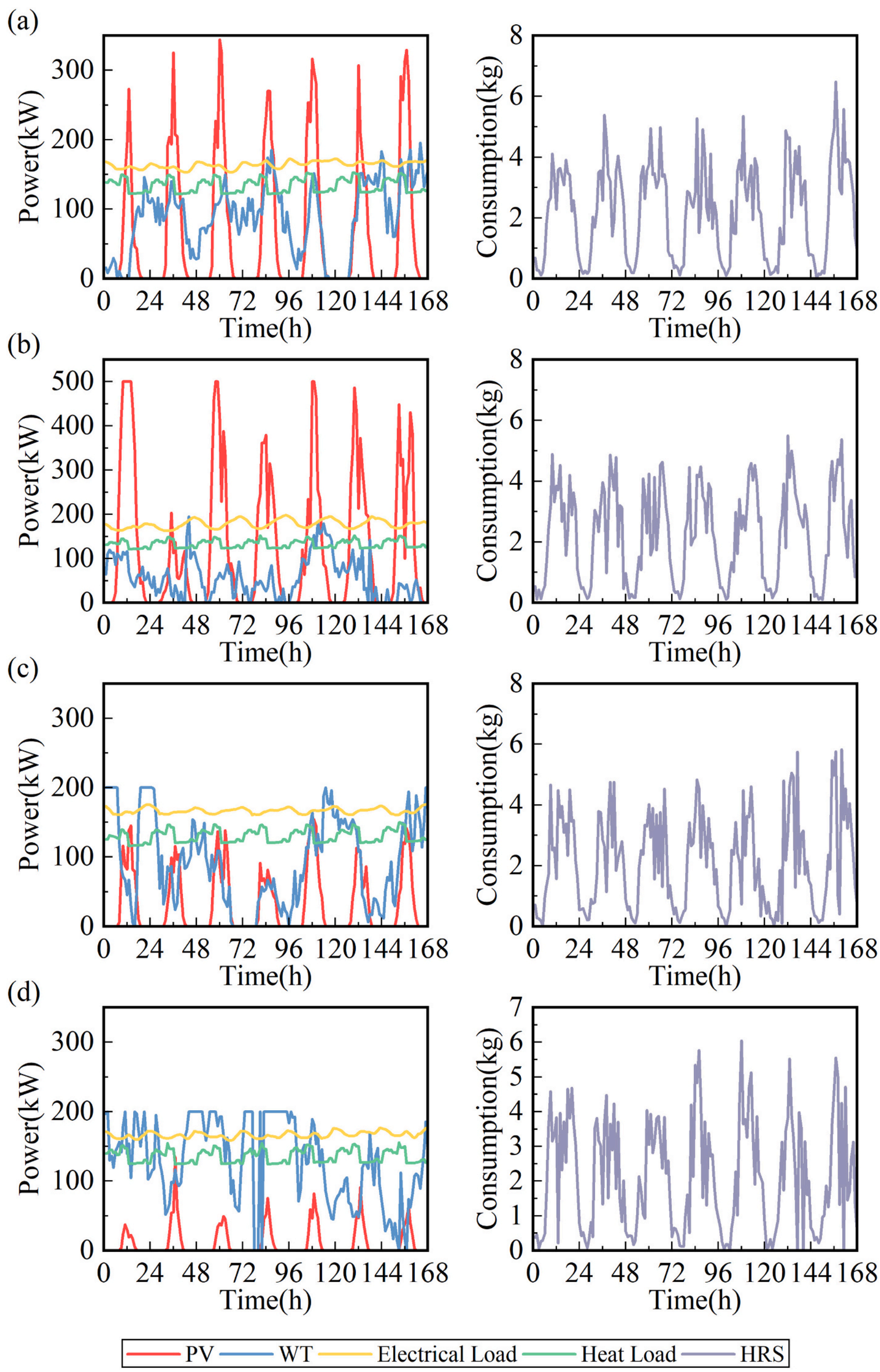

Fig. 6. Typical daily source load curve (a) scenario 1; (b) scenario 2; (c) scenario 3; (d) scenario 4.

Table 8
Results of ANOVA in cost (three factors).

Source	Contribution	DF	Adj SS	Adj MS	F-value	P-value
Scenario	66.25%	2	51,350,112,254	25,675,056,127	5.35	0.158
P_{el}	14.66%	2	11,359,287,818	5,679,643,909	1.18	0.458
P_{fc}	6.7%	2	5,193,076,330	2,596,538,165	0.54	0.649
Error	12.39%	2	9,605,287,631	4,802,643,816	/	/
Total	1	8	77,507,764,033	/	/	/

Table 9
Results of ANOVA in efficiency (three-factors).

Source	Contribution	DF	Adj SS	Adj MS	F-value	P-value
Scenario	79.04%	2	0.000098	0.000049	16.59	0.057
P_{el}	4.84%	2	0.000006	0.000003	1.08	0.481
P_{fc}	10.48%	2	0.000013	0.000007	2.20	0.312
Error	4.84%	2	0.000006	0.000003	/	/
Total	1	8	0.000124	/	/	/

Table 10
Results of ANOVA in ESLP (three-factors).

Source	Contribution	DF	Adj SS	Adj MS	F-value	P-value
Scenario	89.81%	2	0.005777	0.002888	86.19	0.011
P_{el}	1.2%	2	0.000077	0.000039	1.15	0.465
P_{fc}	7.95%	2	0.000512	0.000256	7.64	0.116
Error	1.04%	2	0.000067	0.000034	/	/
Total	1	8	0.006433	/	/	/

In summary, when balancing cost, system comprehensive energy efficiency, and ESLP, it is necessary to consider their respective variation characteristics and the interrelationships among the three. At this point, subjective judgment is challenging, and it is essential to seek potential correlations among the data through objective methods to determine an optimal operating strategy for this typical scenario.

3.3. Selection of optimal solution

In this study, each solution within the Pareto solution set obtained in the previous subsection is ranked by TOPSIS based on entropy weight method to obtain the required best optimal dispatch strategy. The weight calculation results for the three objectives across four typical scenarios are presented in Table 11.

The optimization results are sorted by TOPSIS based on the calculated entropy weights. Due to the large number of solution sets, the ranking results are not presented here. Instead, only the selected optimal solutions in each typical scene are listed. The optimal solution is shown in Table 12.

According to the values of decision variables corresponding to the filtered optimal solutions, the system operation after optimized dispatch is plotted in Figs. 8 and 9. In these plots, the positive value of the power axis represents the external power output of the device, and the negative value represents the power consumption of the device.

As can be seen from the figure, under the four typical scenarios, the system operates smoothly and ensures continuous energy supply. For instance, in Fig. 8(a), when wind and solar resources are abundant, PEMEL and PEMFC operate alternately to balance the electric energy within the microgrid. Throughout the entire operational cycle, the output and consumption of electric energy exhibit symmetry about the X-axis, with consistent fluctuation trends. Similarly, when wind and solar resources are scarce, as depicted in Fig. 8(c), PEMEL and PEMFC still operate alternately. However, there is a noticeable shortfall in power generation during this period, resulting in an increase in ESLP. Nonetheless, the overall trend of power output and consumption remains consistent.

Fig. 9 shows that in the four typical scenarios, the hydrogen and heat demand is adequately met, with no apparent instances where the demand exceeds the supply. To provide further insights, a comparison of the original operation for the four typical scenarios is plotted, as illustrated in Fig. 10.

The figure shows that in Scenario 1, there is no significant change in each index before and after system optimization. This is because under this climate condition, each device in the system has reached the optimal state during normal operation and no further optimization is needed. Under Scenario 2, after optimized dispatch, the system operating cost is reduced by 17.53%, while the ESLP is only increased by 0.55%, and the comprehensive energy efficiency is reduced by 0.13%. In the case of insufficient scenery resources, such as Scenarios 3 and 4, the optimized operation cost has a reduction. Under Scenario 3, due to the lack of landscape resources, the comprehensive energy efficiency of the system is increased by 0.71% and the ESLP is increased by 4.14% while the operating cost is reduced by 41.56%. Under Scenario 4, the wind and solar resources are at a medium level, the operating cost is reduced by

Table 11
Indicator weights under typical days.

Object	Information entropy e	Information utility value d	Weights (%)
(a) Scenario 1			
Efficiency	0.933	0.067	40.377
Cost	0.969	0.031	18.499
ESLP	0.932	0.068	41.124
(b) Scenario 2			
Efficiency	0.961	0.039	27.913
Cost	0.969	0.031	22.745
ESLP	0.932	0.068	49.342
(c) Scenario 3			
Efficiency	0.963	0.037	26.813
Cost	0.968	0.032	23.673
ESLP	0.932	0.068	49.514
(d) Scenario 4			
Efficiency	0.974	0.026	24.445
Cost	0.977	0.023	21.611
ESLP	0.943	0.057	53.944

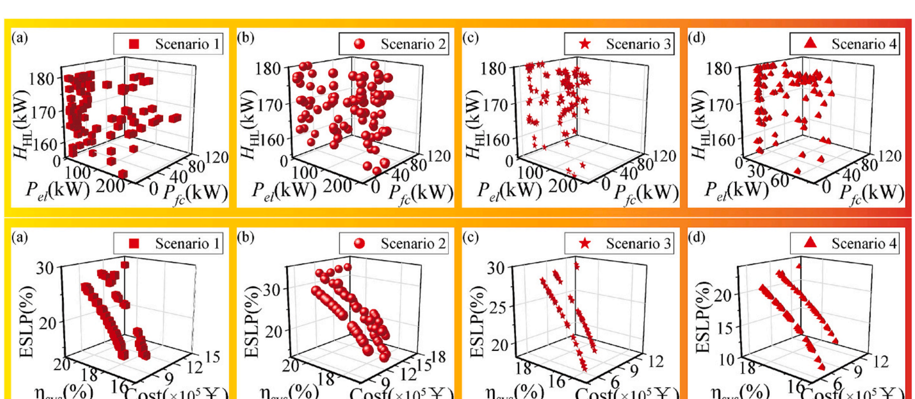

Fig. 7. The Pareto front in different scenarios (a) scenario 1; (b) scenario 2; (c) scenario 3; (d) scenario 4.

Table 12
Optimal solution for different scenarios.

Scenario	Cost (¥)	Efficiency (%)	ESLP (%)
1	1,002,697.34	16.86	14.94
2	1,045,305.80	16.66	16.42
3	538,554.96	16.70	19.02
4	523,033.05	16.70	12.50

46.13%, the comprehensive energy efficiency of the system is increased by 0.61%, and the ESLP is only increased by 0.93%.

By combining the analysis of Figs. 8 and 10, we can observe that when wind and solar power generation is abundant, all devices operate near their optimal state, and the improvement brought by the proposed optimization strategy is not significant. Consequently, there is no notable reduction in aging costs and replacement costs, leading to an overall negligible improvement in economic efficiency. However, when wind and solar power generation is insufficient or even scarce, the devices operate under conditions of frequent fluctuations. In this scenario, the proposed optimization strategy effectively suppresses these fluctuations, significantly reducing aging and replacement costs, resulting in a substantial decrease in total costs, while having minimal impact on system efficiency and stability.

In summary, the proposed optimization dispatch scheme can effectively reduce the operating costs of the system under annual climatic conditions without significantly affecting the efficiency and ESLP of the microgrid.

3.4. *Analysis of solution*

3.4.1. *Economic sensitivity analysis of solution*

In Section 2.2, we developed a devices degradation model and incorporated it into the cost-decision framework for operational optimization. To further elucidate the impact of this factor on the optimization results, two comparative experiments were designed. A specific analysis is conducted using Scenario 1 as an illustrative case. Specifically, experiment 1 disregards the influence of equipment degradation on cost. In contrast, experiment 2 approximates the degradation cost based on the equipment's total operational duration. The resultant

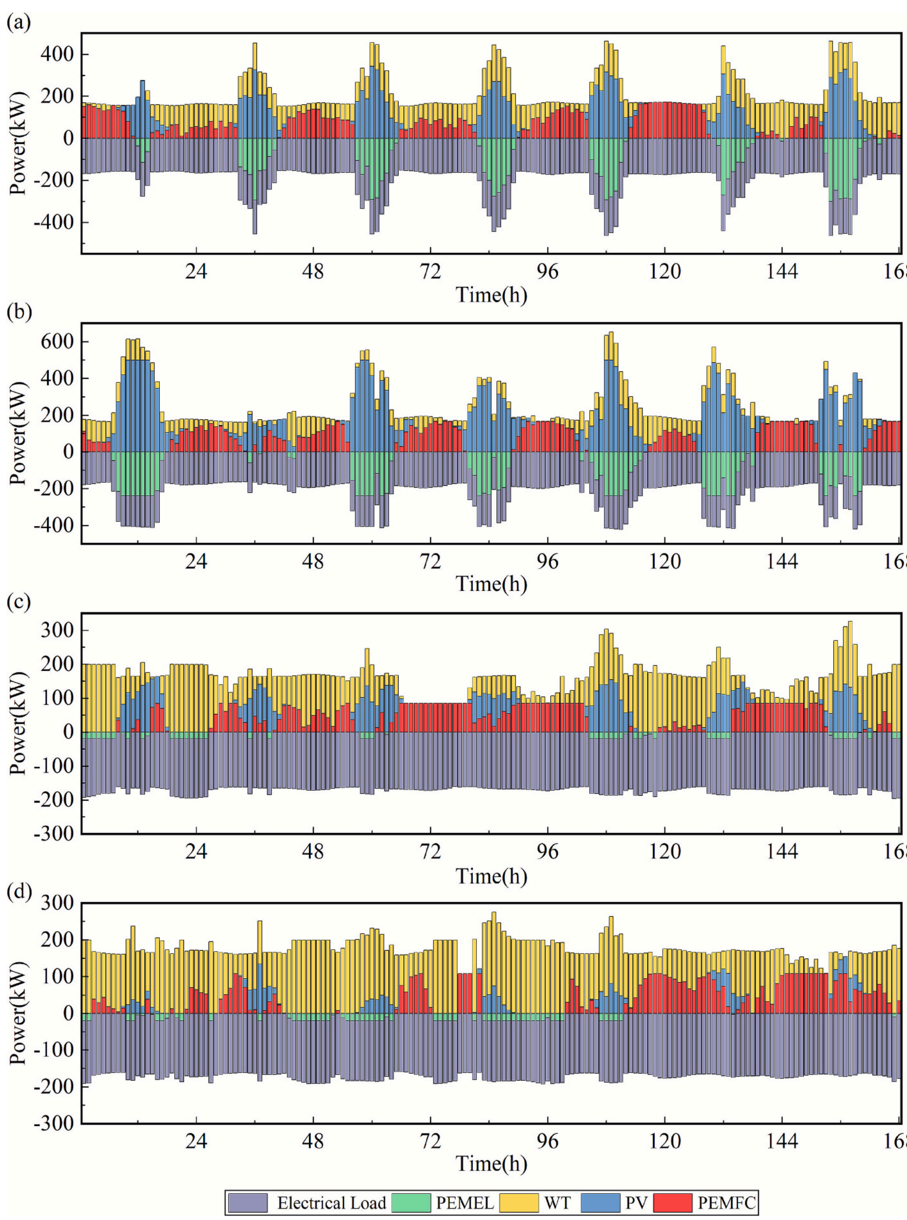

Fig. 8. Operating situation of 168 h under different scenarios (a) scenario 1; (b) scenario 2; (c) scenario 3; (d) scenario 4.

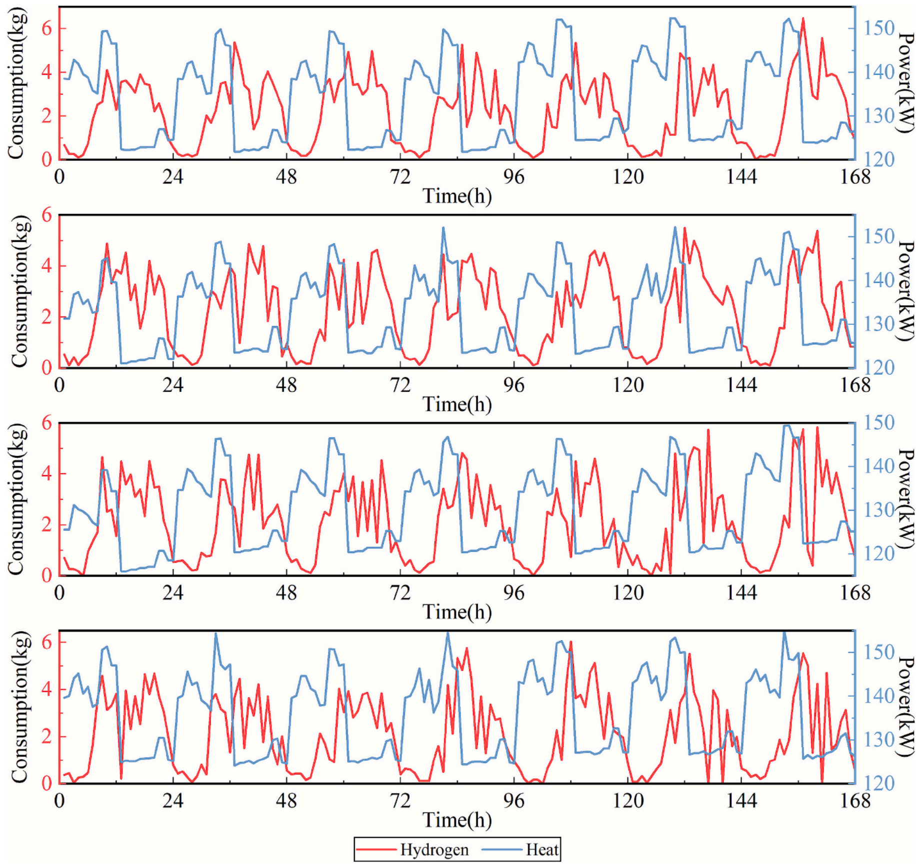

Fig. 9. Demand of hydrogen and heat (a) scenario 1; (b) scenario 2; (c) scenario 3; (d) scenario 4.

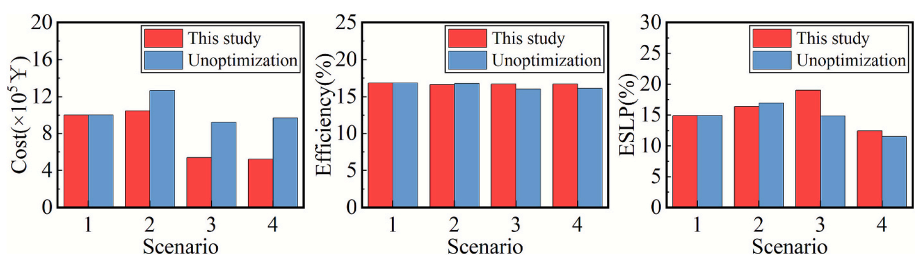

Fig. 10. Comparison of operating results in typical scenarios.

optimal solutions are presented in Table 13.

As observable from the table, a substantial reduction in total cost is achieved when aging costs are entirely disregarded. This implies that degradation cost constitutes a primary component of the operational expenditure and cannot be neglected. Concurrently, the enhancement in efficiency is accompanied by a significant decline in system stability. When degradation costs are crudely estimated, this fixed, coarse approximation results in more aggressive equipment operation, thereby yielding higher system efficiency. However, this approach also leads to a significant deterioration in operational stability. Therefore, it is essential to incorporate equipment degradation costs into the calculation of system operational expenditure. Furthermore, a more refined degradation model facilitates the identification of optimization strategies that offer superior overall performance.

Table 13
The impact of aging on optimization results.

	Cost/¥	Efficiency/%	ESLP/%
Experiment 1	3.38×10^5	16.96	15.54
Experiment 2	9.44×10^5	18.47	24.02
Scenario 1	1.00×10^6	16.86	14.94

3.4.2. Analysis of solution stability

Given the uncertainty inherent in renewable energy sources, this section aims to evaluate the robustness of the Pareto-optimal solution set under varying operational conditions. A sensitivity analysis approach is adopted, wherein "stress-test" scenarios are constructed to assess the performance of the deterministic solutions. Using Scenario 1 as an illustrative case, the high-stress scenario is constituted by a 30% reduction in wind and solar power output, concurrent with a 20% increase in electricity, hydrogen, and heat load demands. Conversely, the low-stress scenario involves a 20% increase in wind and solar generation, coupled with a 20% reduction in all load demands. The cost-optimal solution, the efficiency-optimal solution (both selected from Fig. 7), and the optimal solution identified in Section 3.3 are subjected to a comparative stability analysis. The results are presented in Table 14.

As evident from Table 14, the solution selected in this research exhibits exceptional stability across various scenarios characterized by

Table 14
Comparative analysis under source-load imbalance conditions.

	Scenario 1	High-stress scenario	Low-stress scenario
Cost-optimal solution	25.35%	37.19%	18.60%
Efficiency-optimal solution	29.03%	45.07%	21.87%
Solution selected in this study	14.94%	23.82%	11.32%

imbalances in wind/solar power generation and load demands. In comparison to the cost-optimal solution, the solution chosen in this study maintains performance fluctuations within 10% under both extreme challenge scenarios stemming from renewable energy uncertainty. Furthermore, when contrasted with the efficiency-optimal solution, the stability of the solution selected in this study is consistently more than double across all scenarios. In summary, the solution proposed in this research can, to a significant extent, effectively address the challenges posed by the uncertainty inherent in renewable energy sources.

4. Conclusions

To solve the problems of low energy efficiency of integrated hydrogen energy utilization system (IHEUS), aggravated equipment aging under fluctuating conditions, and high replacement cost, this paper proposes a multi-objective optimization dispatch scheme considering waste heat recovery and life cycle of IHEUS under off-grid. Firstly, the electric-hydrogen-thermal coupling model of each device in the system was established, and the waste heat was recovered and utilized to improve the comprehensive energy efficiency of the system. Then, a multi-objective optimization model was established by considering the operation cost function, the comprehensive energy efficiency function and the energy supply loss probability (ESLP) function in the life cycle, to evaluate the performance of the system during operation more comprehensively. Finally, the NSGA-III joint entropy weight TOPSIS strategy was used to optimize and sort the designed multi-objective optimization model, and the optimal operation dispatch strategy suitable for off-grid was obtained. The proposed strategy can not only effectively balance the energy utilization and stability requirements of the system, but also improve the economy of the system in practical applications, which provides strong support for energy management in off-grid. The main concluding opinions are as follows:

(1) The two performance indicators, comprehensive energy efficiency, and ESLP, show a certain positive relationship, and when the comprehensive energy efficiency is increased, the ESLP under the corresponding conditions will also be increased. However, for the ideal system, it is desired that the ESLP remains constant or decreases when the comprehensive energy efficiency increases.
(2) PEMEL and PEMFC have the most severe voltage degradation and aging when they are maintained at rated power operation; for PEMEL, the voltage degradation caused by frequent starts and stops is much smaller than that of power fluctuation operation, whereas for PEMFC, the effect of starts and stops on voltage degradation is much larger than that of power fluctuation operation.
(3) Under different typical climate characteristics, the operating cost of the system optimized by NSGA-III is reduced by at least 17.53%. At the same time, the comprehensive energy efficiency is reduced by up to 0.13%, and can even be elevated by 0.61% under certain conditions. And in terms of ESLP, it increases up to 4.14%. This means that the optimized dispatch strategy proposed in this study can effectively improve the economic operation of the system while ensuring a certain degree of system stability.

Moreover, we have observed that, compared to the study by Xu et al. [50], the aging model proposed in this research offers a more detailed performance analysis at the component level. This provides a more robust theoretical foundation for optimizing system components during operation.

It is worth noting that this study did not incorporate potential operational risks of the proposed system. To enhance the accuracy and reliability of the simulations, future research will focus on developing a risk assessment model and further investigating the impact of wind and solar power uncertainties on multi-stage day-ahead and intra-day scheduling.

CRediT authorship contribution statement

Shihao Zhu: Writing – original draft, Software, Investigation, Data curation. **Banghua Du:** Methodology, Investigation. **Peipei Meng:** Validation, Resources, Formal analysis. **Xinyu Lu:** Software, Methodology. **Yang Li:** Writing – review & editing, Validation, Resources. **Changjun Xie:** Writing – review & editing, Supervision, Funding acquisition, Conceptualization. **Leiqi Zhang:** Visualization, Data curation. **Bo Zhao:** Project administration, Conceptualization.

Declaration of competing interest

The authors declare that they have no known competing financial interests or personal relationships that could have appeared to influence the work reported in this paper.

Acknowledgment

This paper is supported by the National Key Research and Development Program of China (No. 2020YFB1506802) and the Key R&D Plan of Hubei Province (2023BAB114).

Data availability

Data will be made available on request.

References

[1] A.K. Bansal, Sizing and forecasting techniques in photovoltaic-wind based hybrid renewable energy system: a review, J. Clean. Prod. 369 (2022) 133376.
[2] S. Han, M. He, Z. Zhao, D. Chen, B. Xu, J. Jurasz, F. Liu, H. Zheng, Overcoming the uncertainty and volatility of wind power: day-ahead scheduling of hydro-wind hybrid power generation system by coordinating power regulation and frequency response flexibility, Appl. Energy 333 (2023) 120555.
[3] M. Shi, W. Wang, Y. Han, Y. Huang, Research on comprehensive benefit of hydrogen storage in microgrid system, Renew. Energy 194 (2022) 621–635.
[4] S. Sikiru, T.L. Oladosu, T.I. Amosa, J.O. Olutoki, M.N.M. Ansari, K.J. Abioye, Z. U. Rehman, H. Soleimani, Hydrogen-powered horizons: transformative technologies in clean energy generation, distribution, and storage for sustainable innovation, Int. J. Hydrogen Energy 56 (2024) 1152–1182.
[5] V.M. Avargani, S. Zendehboudi, N.M.C. Saady, M.B. Dusseault, A comprehensive review on hydrogen production and utilization in North America: prospects and challenges, Energ. Conver. Manage. 269 (2022) 115927.
[6] L. Ge, B. Zhang, W. Huang, Y. Li, L. Hou, J. Xiao, Z. Mao, X. Li, A review of hydrogen generation, storage, and applications in power system, J. Energy Storage 75 (2024) 109307.
[7] O. Erixno, N. Abd Rahim, F. Ramadhani, N.N. Adzman, Energy management of renewable energy-based combined heat and power systems: a review, Sustain Energy Technol Assess 51 (2022) 101944.
[8] M. Tahir, S. Hu, T. Khan, H. Zhu, Sustainable hybrid station design framework for electric vehicle charging and hydrogen vehicle refueling based on multiple attributes, Energ. Conver. Manage. 300 (2024) 117922.
[9] X. Sun, X. Cao, M. Li, Q. Zhai, X. Guan, Seasonal operation planning of hydrogen-enabled multi-energy microgrids through multistage stochastic programming, J. Energy Storage 85 (2024) 111125.
[10] N. Endo, E. Shimoda, K. Goshome, T. Yamane, T. Nozu, T. Maeda, Construction and operation of hydrogen energy utilization system for a zero emission building, Int. J. Hydrogen Energy 44 (29) (2019) 14596–14604.
[11] I.A. Hassan, H.S. Ramadan, M.A. Saleh, D. Hissel, Hydrogen storage technologies for stationary and mobile applications: review, analysis and perspectives, Renew. Sustain. Energy Rev. 149 (2021) 111311.

[12] F. Alasali, M.I. Abuashour, W. Hammad, D. Almomani, A.M. Obeidat, W. Holderbaum, A review of hydrogen production and storage materials for efficient integrated hydrogen energy systems, Energy Sci. Eng. 12 (2024) 1934–1968.
[13] D. Zhang, H. Zhu, H. Zhang, H.H. Goh, H. Liu, T. Wu, An optimized design of residential integrated energy system considering the power-to-gas technology with multi-functional characteristics, Energy 238 (2022) 121774.
[14] G. Pan, W. Gu, Y. Lu, H. Qiu, S. Lu, S. Yao, Optimal planning for electricity-hydrogen integrated energy system considering power to hydrogen and heat and seasonal storage, IEEE Trans. Sustainable Energy 11 (4) (2020) 2662–2676.
[15] A. Rabiee, A. Keane, A. Soroudi, Technical barriers for harnessing the green hydrogen: a power system perspective, Renew. Energy 163 (2021) 1580–1587.
[16] Q. Feng, G. Liu, B. Wei, Z. Zhang, H. Li, H. Wang, A review of proton exchange membrane water electrolysis on degradation mechanisms and mitigation strategies, J. Power Sources 366 (2017) 33–55.
[17] F.N. Khatib, T. Wilberforce, O. Ijaodola, E. Ogungbemi, Z. El-Hassan, A. Durrant, J. Thompson, A.G. Olabi, Material degradation of components in polymer electrolyte membrane (PEM) electrolytic cell and mitigation mechanisms: a review, Renew. Sustain. Energy Rev. 111 (2019) 1–14.
[18] S.H. Frensch, F. Fouda-Onana, G. Serre, D. Thoby, S.S. Araya, S.K. Kær, Influence of the operation mode on PEM water electrolysis degradation, Int. J. Hydrogen Energy 44 (57) (2019) 29889–29898.
[19] A. Weiß, A. Siebel, M. Bernt, T.H. Shen, V. Tileli, H.A. Gasteiger, Impact of intermittent operation on lifetime and performance of a PEM water electrolyzer, J. Electrochem. Soc. 166 (8) (2019) F487–F497.
[20] T. Ous, C. Arcoumanis, Degradation aspects of water formation and transport in proton exchange membrane fuel cell: a review, J. Power Sources 240 (2013) 558–582.
[21] P.C. Okonkwo, O.O. Ige, P.C. Uzoma, W. Emori, A. Benamor, A.M. Abdullah, Platinum degradation mechanisms in proton exchange membrane fuel cell (PEMFC) system: a review, Int. J. Hydrogen Energy 46 (29) (2021) 15850–15865.
[22] M. Dhimish, R.G. Vieira, G. Badran, Investigating the stability and degradation of hydrogen PEM fuel cell, Int. J. Hydrogen Energy 46 (74) (2021) 37017–37028.
[23] P. Ren, P. Pei, Y. Li, Z. Wu, D. Chen, S. Huang, Degradation mechanisms of proton exchange membrane fuel cell under typical automotive operating conditions, Prog. Energy Combust. Sci. 80 (2020) 100859.
[24] Z. Li, Y. Xia, Y. Bo, W. Wei, Optimal planning for electricity-hydrogen integrated energy system considering multiple timescale operations and representative time-period selection, Appl. Energy 362 (2024) 122965.
[25] Y. Wang, J. Wang, M. Gao, D. Zhang, Y. Liu, Z. Tan, J. Zhu, Cost-based siting and sizing of energy stations and pipeline networks in integrated energy system, Energy Convers. Manag. 235 (2021) 113958.
[26] Y. Ma, H. Wang, F. Hong, J. Yang, Z. Chen, H. Cui, J. Feng, Modeling and optimization of combined heat and power with power-to-gas and carbon capture system in integrated energy system, Energy 236 (2021) 121392.
[27] J. Zhou, Y. Wu, Z. Zhong, C. Xu, Y. Ke, J. Gao, Modeling and configuration optimization of the natural gas-wind-photovoltaic-hydrogen integrated energy system: a novel deviation satisfaction strategy, Energ. Conver. Manage. 243 (2021) 114340.
[28] H. Dong, Z. Shan, J. Zhou, C. Xu, W. Chen, Refined modeling and co-optimization of electric-hydrogen-thermal-gas integrated energy system with hybrid energy storage, Appl. Energy 351 (2023) 121834.
[29] M. Nasser, H. Hassan, Techno-enviro-economic analysis of hydrogen production via low and high temperature electrolyzers powered by PV/Wind turbines/Waste heat, Energ. Conver. Manage. 278 (2023) 116693.
[30] Y. Lan, J. Lu, L. Mu, S. Wang, H. Zhai, Waste heat recovery from exhausted gas of a proton exchange membrane fuel cell to produce hydrogen using thermoelectric generator, Appl. Energy 334 (2023) 120687.
[31] C. Xu, Y. Ke, Y. Li, H. Chu, Y. Wu, Data-driven configuration optimization of an off-grid wind/PV/hydrogen system based on modified NSGA-II and CRITIC-TOPSIS, Energ. Conver. Manage. 215 (2020) 112892.
[32] Z. Liu, Y. Cui, J. Wang, C. Yue, Y.S. Agbodjan, Y. Yang, Multi-objective optimization of multi-energy complementary integrated energy systems considering load prediction and renewable energy production uncertainties, Energy 254 (2022) 124399.
[33] B. Du, S. Zhu, W. Zhu, X. Lu, Y. Li, C. Xie, B. Zhao, L. Zhang, G. Xu, J. Song, Energy management and performance analysis of an off-grid integrated hydrogen energy utilization system, Energ. Conver. Manage. 299 (2024) 117871.
[34] L. Wang, W. Cai, Y. He, T. Peng, J. Xie, L. Hu, L. Li, Equipment-process-strategy integration for sustainable machining: a review, Front. Mech. Eng. 18 (3) (2023) 36.
[35] X. Lu, B. Du, S. Zhou, W. Zhu, Y. Li, Y. Yang, C. Xie, B. Zhao, L. Zhang, J. Song, Z. Deng, Optimization of power allocation for wind-hydrogen system multi-stack PEM water electrolyzer considering degradation conditions, Int. J. Hydrogen Energy 48 (15) (2023) 5850–5872.
[36] Y. Pu, Q. Li, X. Zou, R. Li, L. Li, W. Chen, H. Liu, Optimal sizing for an integrated energy system considering degradation and seasonal hydrogen storage, Appl. Energy 302 (2021) 117542.
[37] J. Sim, M. Kang, K. Min, E. Lee, J.Y. Jyoung, Effects of carbon corrosion on proton exchange membrane fuel cell performance using two durability evaluation methods, Renew. Energy 190 (2022) 959–970.
[38] X. Lyu, J. Foster, R. Rice, E. Padgett, E.B. Creel, J. Li, et al., Aging gracefully? Investigating iridium oxide ink's impact on microstructure, catalyst/ionomer interface, and PEMWE performance, J. Power Sources 581 (2023) 233503.
[39] H. Zhou, B. Chen, K. Meng, W. Chen, G. Li, Z. Tu, Experimental investigation of degradation mechanism in proton exchange membrane water electrolyzer under prolonged and severe bubble accumulation condition, Chem. Eng. J. 491 (2024) 152202.
[40] X. Huang, S. Liu, X. Yu, Y. Liu, Y. Zhang, G. Xu, A mechanism leakage model of metal-bipolar-plate PEMFC seal structures with stress relaxation effects, Int. J. Hydrogen Energy 47 (4) (2022) 2594–2607.
[41] Y. Zhao, M. Luo, J. Yang, B. Chen, P.C. Sui, Numerical analysis of PEMFC stack performance degradation using an empirical approach, Int. J. Hydrogen Energy 56 (2024) 147–163.
[42] H. Yazdani, M. Baneshi, M. Yaghoubi, Techno-economic and environmental design of hybrid energy systems using multi-objective optimization and multi-criteria decision making methods, Energ. Conver. Manage. 282 (2023) 116873.
[43] H. Ma, Y. Zhang, S. Sun, T. Liu, Y. Shan, A comprehensive survey on NSGA-II for multi-objective optimization and applications, Artif. Intell. Rev. 56 (12) (2023) 15217–15270.
[44] F. Wang, H. Zhang, A. Zhou, A particle swarm optimization algorithm for mixed-variable optimization problems, Swarm and Evolutionary Computation 60 (2021) 100808.
[45] L.E. Lwakatare, A. Raj, I. Crnkovic, J. Bosch, H.H. Olsson, Large-scale machine learning systems in real-world industrial settings: a review of challenges and solutions, Inf. Softw. Technol. 127 (2020) 106368.
[46] K. Deb, H. Jain, An evolutionary many-objective optimization algorithm using reference-point-based nondominated sorting approach, part I: solving problems with box constraints, IEEE Trans. Evol. Comput. 18 (4) (2013) 577–601.
[47] M.R. Elkadeem, A. Younes, S.W. Sharshir, P.E. Campana, S. Wang, Sustainable siting and design optimization of hybrid renewable energy system: a geospatial multi-criteria analysis, Appl. Energy 295 (2021) 117071.
[48] Y. Wang, X. Wang, H. Yu, Y. Huang, H. Dong, C. Qi, N. Baptiste, Optimal design of integrated energy system considering economics, autonomy and carbon emissions, J. Clean. Prod. 225 (2019) 563–578.
[49] P. Chen, Effects of the entropy weight on TOPSIS, Expert Syst. Appl. 168 (2021) 114186.
[50] C. Xu, X. Wu, Z. Shan, Q. Zhang, B. Dang, Y. Wang, F. Wang, X. Jiang, Y. Xue, C. Shi, Bi-level configuration and operation collaborative optimization of shared hydrogen energy storage system for a wind farm cluster, J. Energy Storage 86 (2024) 111107.